MESOSCALE WATER WETTING OF LOW-DENSITY FIBROUS STRUCTURES: EXPERIMENTATION AND SIMULATION

D. S. Keller[1], H. Abedsoltan[1], J. Reid[1] and L. Yin[2]

[1] Miami University, Department of Chemical, Paper and Biomedical Engineering, Oxford, OH, USA
[2] Beckman Institute, University of Illinois at Urbana-Champaign, Urbana, IL, USA

ABSTRACT

This paper describes the investigation of the water absorption behavior of low density, fibrous kitchen towels at dimensions from 10^{-3} mm to 10^2 mm. The investigation involved both the experimental observation of radial wetting from a point source and the numerical simulation of the wetting using X-ray 3D microscopic data sets obtained from the same set of towel papers that were representative of conventional and premium products. The overarching aim was to examine the validity of the simulation, based on fundamental surface energetics of the condensed phases, in predicting the local flow patterns that are dependent on various structural features found in retail kitchen towel products. This study explored the relationships between local structural properties, including thickness, grammage, apparent density and out of plane deformation. Experimental results examined the local flow velocity in and around the various structural features of conventional and structured towels. Analysis of both experimental and simulated liquid regions included calculation of water absorbency capacity, aspect ratio, density analysis and through holes.

D. S. Keller, H. Abedsoltan, J. Reid and L. Yin

INTRODUCTION

The interaction of water with lignocellulosic fibers found in paper touches nearly all aspects of papermaking and end usage. Most printing and packaging grades require reduced rate of water penetration to prevent loss of strength, promote the holdout of coatings and inks, or to enhance barrier properties. Conversely, hygienic tissue papers, including facial tissues, napkins, bathroom tissues, and household and away-from-home (AFH) paper towels, require a relatively high rate of liquid absorption to be effective in their end use performance. Paper towel products require seemingly opposing structural characteristics of high bulk for absorbency and handle, and sufficient interfiber bonding to meet dry and wet tensile strength requirements. To achieve this dichotomy, the design of paper towels has inspired paper scientists for the past 100 years. In 1922, W. E. Corbin led his scientific team at the Brown Co. in Berlin, New Hampshire to develop the first wet strengthened AFH hand towel [1]. While Scott Paper Company is considered to have distributed the first hygienic hand towel in 1907 as a creative solution to a manufacturing error, it was not until 1931 that papermakers at that company first introduced an engineered kitchen towel to the market [2]. The creping process was introduced in the 1890's by Dennison Manufacturing Company for decorative papers [3] and was adopted by the Scott Paper Company as a cotton cloth replacement for bandages in World War I [2]. Creping was also applied in other hygienic tissue products for the increased bulk, stretch, and flexibility. In the 1960s, Procter and Gamble (P&G) [4] developed the nested and point to point embossing processes for laminating tissues into multiple plies, greatly increasing the liquid absorption capacity. In the same decade, P&G also introduced the through air drying (TAD) process which created a heterogeneous pattern of bulked and densified regions within the paper structure [5, 6]. The TAD structure further improves absorbency, softness, and flexibility of the product, while enhancing tensile strength. The retail demand and competition for the tissue and towel market share have resulted in hundreds of patents claiming process and design developments to improve product quality, performance, and process efficiency. Thus, contemporary products are highly engineered using many distinct unit operations to attain products that are generally distinct from their competitors. With an expected compound annual growth rate of 5%, and continued constraints on raw materials, water, and energy, there continues to be significant scientific interest in understanding the effect that manufacturing and converting processes have on material properties, and how the material properties affect end use performance. This investigation focused on liquid absorbency of paper towels, specifically how the mesoscale structure, from 10^{-5}m to 10^{-2}m, influences local liquid transport. Through numerical modeling and experimental observation and analysis, the local wetting behavior of a range of towel structures was examined.

Characteristics of Contemporary Kitchen Towels

At present, kitchen towels, bathroom tissues and facial tissues are classified according to performance and quality metrics resulting from the methods used in the manufacturing processes. In the US, the three general categories are conventional, near premium and premium. Kitchen towels that occupy the conventional market segment are made on tissue machines that use a technology referred to as light dried crepe (LDC), conventional wet pressed (CWP) or dry creped technology (DCT) [7, 8]. For this process, the wet web is formed between two wires or a wire and a felt and then is pressed against a Yankee cylinder that is used to evaporate the remaining water. The dried web is removed from the dryer by a creping process that debonds the web and compresses it in the machine direction. The creping blade buckles or bulks the web to produces ridge lines in the cross machine direction. This increases the stretch to failure and reduces the flexural stiffness of the web, which in turn imparts softness and absorbency in the final product. The creped web may then be calendered before it is wound on the parent roll. The manufacture of premium paper towels requires more complex processing that involves "structuring" of the web with one or more engineered features. Contemporary processes used to structure tissue apply a variety of proprietary technologies, i.e. TAD, eTAD, QRT, UCTAD, NTT, and ATMOS, that essentially form structural features, such as domes, knuckles or patterns, in the wet web before or during drying [7, 8]. A patterned fabric or belt with finely spaced openings is used to support the wet web as hot air is passed through the web, thereby drying it by convection. Through air drying (TAD) was the first and is the most recognized process for introducing structures that produce a heterogeneous pattern of densified and bulked regions at dimensions on the same order as the furnish fiber length. These structures are also more resistant to deformation when they were wet. In most cases, web structuring is followed by a dry creping process that causes further inplane compression of the structure. The result is a product that balances bulk and strength with better absorbency and softness as compared to conventional products of the same grammage. It is the examination of these fine structural features, and their effect on liquid wetting and absorbency that motivated this investigation.

BACKGROUND

Absorption and Wetting in Complex Structures

The imbibition of a liquid into an open porous solid material, such as paper, involves the complex interaction dependent on fluid dynamics and the rheological behavior of the liquid, the morphology of the internal pore space, and the chemical

interaction at the interfaces between the three phases. The interaction may also involve vapor deposition in advance of the spreading liquid front and any changes in the solid material that may occur upon exposure to the liquid such as liquid absorption or dissolution of the solid phase. Since so many natural or scientific phenomena depend on this three-phase interaction, the science of wetting and adhesion has expanded into its own branch of materials science, commencing in earnest with the publication by T. Young [9] relating liquid and solid surface energies to the contact angle formed in vapor. Macroscopic observations such as the contact angle formed when the liquid first contacts the porous surface, the rate of absorption into the structure, and the capacity that a structure can hold depend on many morphological and chemical properties of the solid material. Ideally, the liquid is pure and well-defined, the solid phase is composed of an insoluble material with uniform chemistry forming a porous structure with simple and well defined geometry. For the material systems encountered by paper scientists in their investigation of the many interactions of liquids with consolidated fibrous structures, systems that approach ideal conditions are exceedingly rare. Complications result from the complexity of size, shapes and contortion of the fibers within the web creating a tortuous capillary system with obstructions and terminating channels. Pressing, drying and calendering of this heterogeneous structure result in non-uniform density in all three dimensions. Tissue and towel papers are subject to additional processing steps, such as structuring and creping, that further contribute to structural complexity. Imbibition of water into the structure can cause dimensional changes in the fibers [10] and movement of fibers within the structure [11, 12] as bonds are broken and internal stress is released. The wetting energetics is further complicated by the heterogeneity of fiber surface chemistry and the presence of soluble impurities or additives that change the probe liquid surface tension and may readsorb onto the fiber surface as the liquid advances through the structure. For these reasons, both the modeling and the interpretation of wetting experimental results for the interaction of water with paper, especially hygienic papers, remain a difficult pursuit.

Measurement of Liquid Absorption in Tissue and Towels Towel Grades

While the focus of this investigation was to examine the local effect of web structures such as fiber flocs, creping, structured features and embossments, on liquid spreading in paper towels, it is the accumulation of local behavior that forms the macroscopic or bulk absorbency in the final product where the results find application. There are standard tests that use different approaches for measuring the bulk absorbency and holding capacity of towel and tissue products. TAPPI T432 [13] measures absorbency using visual determination of the absorption of a fixed volume of liquid (100 μL) is delivered to the sample surface by syringe or dropper.

ISO Standard 12625–8 [14] uses the change in buoyancy to measure absorption time as a 5 g sample is fully immersed in a water bath. Capacity is determined by the final weight of the fully wetted paper after a 60 second drainage time.

Dynamic Liquid Absorbency Testing

The liquid absorbency behavior of low density papers is generally tested using instrument designs that measure either unidirectional or radial wicking [15]. Liquid may be delivered in a fixed volume (finite reservoir) or from a continuous supply (infinite reservoir), as shown in Figure 1. Figure 1A illustrates unidirectional wicking from an infinite reservoir as used in the Klemm Method [16], where the height of the advancing wet/dry boundary is recorded as a function of time. Figure 1B also shows liquid delivery from an infinite reservoir as the liquid is delivered by an orifice and the radial spreading is either imaged or the imbibed mass is recorded with time. Figure 1C shows the simplest form of finite reservoir testing by observing the radial spreading as a drop of known volume is placed on the surface. The method used in this study is illustrated in Figure 1D where radial spreading is imaged as the liquid is delivered at a controlled volumetric rate (infinite reservoir) up to a maximum volume. Spreading beyond that point is considered as supplied by a finite reservoir. The dynamic wetting of the material can be characterized by measuring the rate at which liquid spreads from the source. A comprehensive review of the experimental methods used to examine wicking in textiles was given by Parada *et al.* [17].

Numerous investigators have applied the horizontal radial spreading approach in the investigation of tissue and towel papers using both finite and infinite reservoir conditions as shown in Figure 1B. The orifice method was first introduced by Reid [18]. Two commercially available instruments automate the method; the Gravimetric Absorbency Tester, (MK/GATS Model 1200, MK/Systems) [19, 20] , and the Absorbency Testing System, (ATS-600, Sherwood Instruments) [21].

Liquid is delivered to a central point in the sample through an orifice in the lower support plate. Rate and capacity are determined gravimetrically. The sample may be restrained on top by another flat plate. Plates may also be recessed to reduce contacting so wicking at the plate-sample interface is avoided. Beuther and Veith [22] demonstrated that the GATS/ATS methods, standardized by the now withdrawn TAPPI T-561 pm-96 [23], yields an unacceptable level of variability attributable to restraining plate composition, sample size and sidedness, and liquid head pressure. Loebker and Sheehan [24] introduced an improved method, referred to as the Capacity and Rate Tester (CRT), by replacing plates with a monofilament support mesh that essentially eliminates artifacts due to the wetting of the plate material at the external boundaries. While these methods provide a representation of the overall rate of wetting and the capacity of uptake,
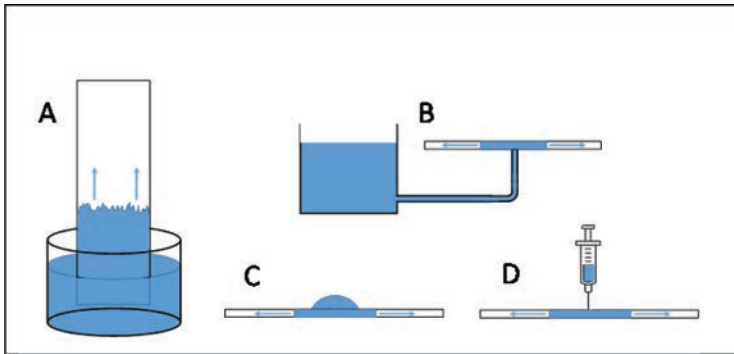
Figure 1. Designs of instruments used to test the in-plane wicking of liquids into thin porous materials. A) Unidirectional wicking from an infinite reservoir. Absorption rate is determined by measuring the length of the advancing wet/dry boundary. B) Radial spreading from a central orifice. Liquid is delivered from an infinite reservoir using only the capillary pressure from the sample. C) Radial spreading from drop delivery of a finite volume of liquid. D) Radial spreading from a volumetrically controlled delivery system. Controlled infinite reservoir flow occurs until a maximum volume is delivered. Thereafter, flow is considered finite reservoir.

they offer no insight into the effects that structural heterogeneity has on liquid transport at the scale of features found in tissue and towel papers. To explore wetting behavior at smaller dimensions, various imaging methods have been used to quantify the non-uniformity of dynamic wetting that occurs in fibrous textile materials [17].

Beuther *et al.* [25] used X-radiographic imaging to record the advancing fluid front in unidirectional wicking of towel samples. They found a favorable correlation between the linear spreading results and those obtained using a radial spreading CRT type orifice tester. The non-uniformity of local wetting rate and the distribution of water within the wetted region are evident in the radiographic images shown in their results. The pattern is consistent with the sample tested, i.e. single-ply Scott towel, and is illustrative of the role that local structure has in liquid transport rate. Gabrielsson *et al.* [26] introduced infrared imaging of radial spreading in towel papers using a GATS type orifice tester with an infrared transparent window as the top plate. As liquid spread into the towel samples, the infrared camera sensed the heat of wetting at the wet/dry boundary. Irregular flow patterns were readily observed as the water spread from the point source through the heterogeneous structure of embossments and creping. Dynamic absorption rates were determined when the samples were subjected to different levels of

compression. Asymmetry of the wetted region was observed for a CWP dry-creped towel, with faster wetting in the cross machine direction, suggested preferential flow parallel to creping lines. Olejnik *et al.* [27] developed the eXtended Liquid Penetration Analyzer to image the liquid penetration through the Z-direction of papers. The sample is held horizontally and a fixed volume of liquid was delivered to the underside of the paper. A CCD camera held above the sample recorded changes in the optical properties of the paper. This method was applied to towel tissue papers to observe the in-plane spreading of the water beyond the initial perimeter of delivery [28]. From acquired images, the wetted area, perimeter, and principal axes and orientation of area were calculated. A water absorption index was also calculated as the ratio of the mass of the absorbed water to the dry mass of the wetted area for the sample. Compactness values, defined as the ratio of the area of the object to the area of a circle with a perimeter of the same length, were calculated as the wetted area expanded. Image analysis of wetted areas was used by Morais *et al.* [29] to study the effect of large (deco) and small (micro) embossing patterns on tissue paper absorbency. They compared liquid spreading kinetics for various samples by analyzing the wet/dry perimeter as a function of time using optical reflectance [30]. While the statistical analysis of the perimeter provided some insight into the differences in behavior, more importantly, the spreading kinetics was strongly influenced by embossed features, paper formation and the orientation of micro embossments.

The aim of this investigation was to extend the analysis of radial spreading into much lower liquid volumes and much finer spatial dimensions than previously tested. By doing so, the effects that fiber flocs, TAD structures, creping and embossments have on spreading would be revealed. The purpose was to observe the local rate of wetting and how it is influenced by the density non-uniformities caused by the various structural features found in tissues and towels.

Surface Energy of Lignocellulosic Fibers

It is understood that the surface energetics, and hence wettability behavior, of individual fibers within the paper towel structure depend on the chemistry of the pulp and the additives used in the papermaking process. The wetting model developed in this study uses the interfacial energies of the fiber and the absorbed liquid to determine the energetic favorability for the liquid to spread within the structure. As such, the selection of surface energy values that are representative of fibers within the towel samples under the conditions of testing is essential for a model to properly represent wetting behavior and especially so that a comparison with experimental results can be performed. What follows is a review of the literature to justify selection of specific energetic parameters the fibers used in the wetting model.

A comprehensive review of the topic of surface energetics, contact angle and wettability with regard to lignocellulosic fibers is provided by Hubbe *et al.* [31]. For retail kitchen towels, contemporary pulps are typically made from bleached kraft softwood and hardwood blends. These may be comprised of varying amounts of virgin and recovered fibers. Away-from-home paper towels may also be made from unbleached kraft fibers, although these products were not included in the present study. The presence of wet strengthening aids, dyes, or other chemicals adsorbed on the fiber surfaces, whether intended or not, are also expected to affect surface energy.

The surface energy of the individual kraft fibers has been the subject of various investigations [32–36]. A modified Wilhelmy [37] technique introduced by Miller and Young [38] was the most common method used to measure dynamic wettability. The method involves making precise measurements of the force required to retract individual fibers immersed in a liquid, e.g. deionized water, through the liquid/vapor interface and simultaneously recording the tri-phase contact angle (advancing). Table 1 provides results from the literature for testing contact angle and surface energy for kraft pulped fibers. The results from the various investigators suggest that the water/air contact angle for individual bleached kraft fibers after air dried conditioning ranged from 11° to 23°. The contact angle for unbleached fibers that contain appreciable amounts of lignin appears to be higher,

Table 1 Contact Angles and Surface Energies of Kraft Fibers

Kraft Pulped Fibers	*Bleached or Unbleached*	*Contact Angle with water,* $\theta°_{avg}$	*Total Surface Energy,* mJ·m^{-2}	*Reference*
Douglas Fir (8.3% lignin)	UB	52°	44.4	Young [32]
Loblolly Pine : *AD	B	11.0°		Hodgson and Berg [33]
Douglas Fir: *AD	B	20.3°		
Douglas Fir: *OD	B	38.5°		
Loblolly Pine:*OD (0.2% lignin)	B	20.8°		Klungness [34]
Northern Softwood	B	17°	71.3	Yoshinaga *et al.* [35]
Softwood	B, UB	23°, 28°		Jin *et al.* [36]
Eucalypt – *AD	UB	49.4° – 52.8°	43.6 – 44.6	El Omari *et. al.* [39]
Hardwood Fiber: w/ESEM Imaging	B	0°		Liukkonen [40]
*AD – Air Dried 23°C		*OD – Oven Dried 24 h @ 105°C		

in the range of 50° with a total surface energy of about 44 mJ·m^{-2}. Hodgson and Berg [33] reported two important observations germane to this study. First, they found a significant increase in contact angle if fibers were oven dried at 105°C. While they attributed this to self-sizing that is usually associated with mechanical pulps, an alternate explanation may attribute this to dehydration of the cell wall leaving a roughened porous surface with pores filled with air rather than water. Secondly, they reported the relationship between contact angle and absorbency into a fluff pulp pad using a procedure developed by Martinis *et al.* [41], the results of which are shown in Figure 2. It is evident, that fibers with contact angles of less than 20° rapidly wet. For fibers with contact angles of 40°or greater, such as unbleached kraft or oven dried fibers, the wetting time is much slower. For this study, a contact angle of 20° with a surface energy of 70 mJ·mm^{-2} will be used for the numerical wetting simulation.

It is important to note that under experimental conditions the surface energy of a solid may be affected by adsorption of the vapor molecules in advance of the wetting liquid on the non-wetted surface. This may account for the variability of values for kraft fibers reported in the literature. Of course, preconditioning and the equilibrium moisture content within the cell wall at a given relative humidity will also affect the apparent surface energy. As seen in Table 1, wetting surface energy of the fibers increases with the amount of adsorbed water, thereby reducing the contact angle with water.
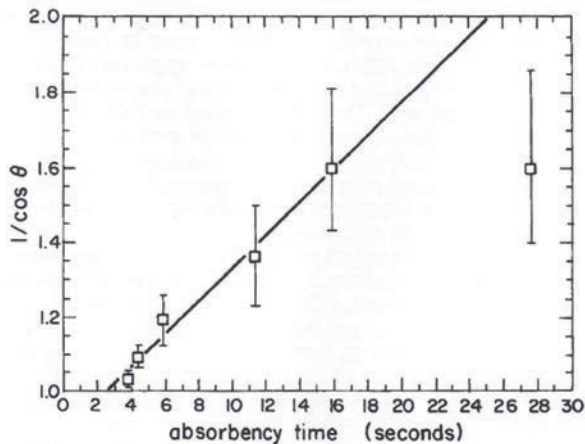
Figure 2. Relationship between single fiber contact angle measured using the modified Wilhelmy technique and fluff pulp absorbency [41]. Redrawn from Hodgson and Berg [33].

D. S. Keller, H. Abedsoltan, J. Reid and L. Yin

Modeling of Liquid Absorption into Thin Fibrous Structures

The transport of liquids within thin fibrous systems, especially textiles and papers was the subject of numerous investigations as reviewed by Pan and Zhong [42] and Patniak *et al.* [43]. The model of Washburn [44] in which the system is approximated by a series of equivalent unidirectional capillaries has been applied by some [15, 45, 46], and criticized by others [47, 48]. The major limitations of this approach are that it requires equivalent capillary diameter as an input, it has no provisions for fiber response to the liquid including absorption that causes swelling, contortion or debonding. Models also do not account for fine scale structure introduced by the many induced features, such as embossments or creping, found in most tissue and towel papers.

Recent investigations have sought to model both the change in stiffness and dimension as lignocellulosic fibers are immersed in water, as well as the dimensional response of paper as a water interface advances through the web. It is well recognized that the fibers absorb water and swell when exposed to water. The imbibition of water into the intrafiber pore structure will in turn have a profound effect on the void space within a fibrous structure [10]. In low density tissue and towel papers, closing of interfiber pore space due to fiber swelling is less of a concern than the change in flexural stiffness of individual fibers and the potential of joint weakening that would result from intrafiber absorption. Although tissue and towel samples are intentionally formed to minimize internal stress, structural deformation can still occur in response to the stresses caused by the advancing interfacial menisci as a liquid is absorbed into the structure. Nasouri *et al.* [11] examined the influence of the change of web stiffness when wet and how separation distance decreases between two like paper sheets as water advances due to capillary rise. They concluded that intrafiber wetting and the effect on web stiffness should be accounted for in wetting model. That study will also be useful for considering wetting of two-ply towels, and the effects of an advancing water front between the plies. Kvik *et al*. [12] investigated the deformation of kitchen towel that occurs as liquid is imbibed into the web. They developed a model based on poroelasticity theory that predicted swelling of the web behind the wetting front of water advancing through the pores by capillary suction. Optical coherence tomography was used to verify the model for standard handsheets and towel samples. These models address the global dynamics of the response of paper samples to the imbibition of water. The deformability of fibers and the fibrous structure upon wetting cannot be discounted in a comprehensive model of wetting in materials such as kitchen towels. However, for the model presented in this study, the structure is assumed to be static and occupy the spatial volume of a dry sample. Consideration is given to the spatial distribution of fibers, the manner in which they conform to induced structures, and the heterogeneity of density. Therefore, the focus of this model is how the local structure at the scale of fiber spatial

geometry affects an advancing liquid front, and not on the hydrodynamics of the liquid transport throughout the fibrous structure during the wicking process.

An important step in modeling liquid flow in tissue and towel structures is to incorporate an accurate representation of the three-dimensional topography into a discretized numerical simulation. Jagannathan *et al.* [49, 50] applied a 3D microscale simulation based on Darcy's law for partially saturated media [51] to analyze the flow in 3D tomographic representations of a nonwoven fabric. This approach was further applied to modelling multi-layered fibrous sheets [52] and an examination of the effects of fiber orientation [53]. Hyväluoma *et al.* [46] used the lattice-Boltzmann method [54] combined with a multiphase model [55] to simulate liquid penetration into paper board. That approach had the advantage of using an X-Ray 3D microscopic (XR-3DM) representation of a real sample as the stationary phase. The model also introduced simple mesoscale cohesive and adhesive interaction parameters to account for the interfacial chemistries of the solid and liquid phases. They tested both unidirectional and radial penetration where the heterogeneity of liquid propagation at the spreading front was observed. The present investigation uses a similar approach by advancing the spreading front based on the summed interaction energy of the neighboring lattice nodes but without the collision operator. Also, hydrodynamics, including liquid rheology, mass balance, evaporation and vapor deposition in advance of the liquid front were neglected.

Numerical Modelling

The inspiration for the numerical model developed in this investigation that is used to simulate the spreading of liquids in low density kitchen towels was found in the works of Cheriet *et al.* [56, 57] and Lukas *et al.* [58, 59] that are based on the foundation given by Ising [60]. The Ising model was first used to describe the change of state of discrete elements when small scale changes, such as temperature or pressure, cause macroscopic changes in a system. The model was specifically applied to the thermal dependency of magnetism where the ferromagnetic state of the bulk system was determined by the magnetic dipole moments, or spins, of each element within a 2D lattice. The state of each element was independent of the bulk system and changed only when its spin state differed from its nearest neighbors. The utility of this approach for application to the switching of elements from void to liquid that occurs when a liquid spreads through a fibrous structures was first introduced by Lukas *et al.* [61–65]. They considered both 2D and 3D lattice systems. Lukas *et al.* [64] postulated that the interaction between elements could be expanded to other energetic systems such as heat transport or interfacial energy. In as such, a replacement of one phase for another for an element within the lattice can occur when the summation of interactions with surrounding neighbors is energetically favorable. From that starting point, they demonstrated the application of

numerical modelling of the transport of moisture through various model systems. Systems included wetting along cylindrical rods [61], wicking through aligned rod bundles [62], and wetting in computer simulated fibrous structures having different levels of in-plane anisotropy [63]. The initial state of a model system was a 2D or 3D lattice with elements being either solid or void and selected elements that were liquids introduced to initiate the simulation. An example of such a system is shown in Figure 3 where the solid phase (white) represents the fibrous structure found in a typical TAD paper towel, imaged using XR-3DM. The blue elements represent the liquid just prior to 3D unidirectional wicking. The red void element found at the liquid-void interface is subject to analysis to determine if it will be changed to liquid based on the interaction energy with all neighboring cells. Input variables for a simulation include interaction energy coefficients for fiber-liquid adhesion and liquid-liquid cohesion, and in some cases a constant representing the gravitational field. For most of the studies that Lukas performed, interaction energies were either approximated or sourced from the literature [59, 64].

Based on the model developed by Lukas *et al.*, Cheriet *et al.* [57, 66] modelled the movement of ink through simulated fibrous structures with densities similar to printing papers. They also simulated the ink seepage using a lattice Boltzmann method, similar to Hyväluoma *et al.* [46], in a 3D lattice ($400 \ \mu m^3$). An algorithm was presented to increase calculation efficiency by reducing the redundancy of exchange energy determination for nearest neighbors. Their approach also focused exchange calculations on only the elements at the liquid / air interface. Once again, that work was limited to computer-generated simulations of fibrous structures.

Considering the 3D Cartesian lattice used for modeling wetting in the complex fibrous structure of paper, the resolution of the elements is significant. While collapsed kraft pulped wood fibers have transverse dimensions in the range of 1 μm to 50 μm, they also have surface asperities and microfibrillar features that are much
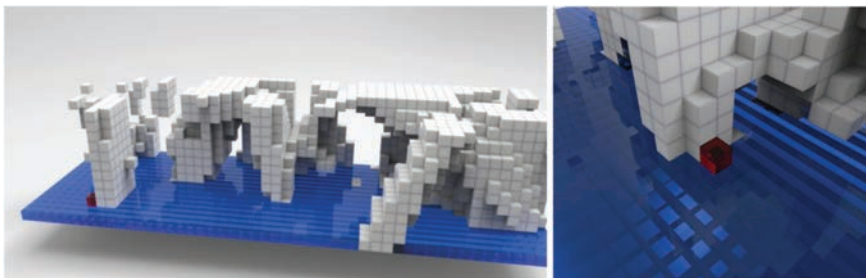
Figure 3. Representation of a region of a XR-3DM data set shown solid-fibers (white) and a liquid-water surface (blue). Each void element that potentially intersects both solid and liquid (red) is tested to determine if the energy of the system is reduced if it converts to liquid. In this way, liquid advances through the structure.
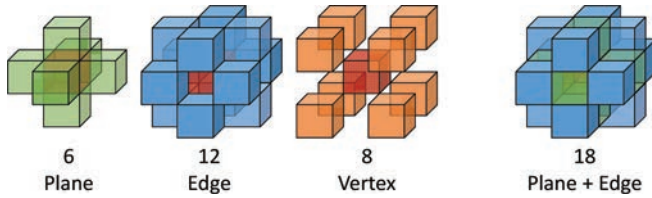
Figure 4. The nearest neighbors in contact with a central element red in a 3D Cartesin space. Six element are in contact with one plane, 12 are in contact with one edge, and eight are in contact with one vertex. In this study elements contact a plane or an edge are considered totaling 18 nearest neighbors.

finer than 1 μm. In order to characterize wetting in towel and tissue papers, the ideal modelling space should span from a submicron resolution though a maximum dimension that encompasses a representative distribution of the structural features of interest. Ideally this would be a data set with scale spanning 5 orders of magnitude in length and containing $\sim 10^{15}$ elements. Since the domain of the structure is discretized into a 3D Cartesian lattice, interfacial interactions with neighbors are incremental in directionality, which limits representation of meniscus curvature that occurs in the natural system. Figure 4 illustrates the neighboring elements in contact with a central element shown in red. In order of proximity, 6 neighbors share one planar surface with the central element, 12 elements share one edge, and 8 share one vertex. Fidelity of the model improves by considering the interactions with more neighbors, although at the cost of additional computational steps. For the present study, neighbors that share one plane and one edge will be used in the model for a total of 18 neighbors.

Energy Minimization Model to Simulate Wicking in Paper Towels

The model developed by Cheriet *et al*. [57, 66] that tested the interaction energetics at the liquid-void interface seemed ideally suited to simulate the spreading of liquid through low density kitchen towels using tomographic data sets obtained from actual samples. Binarization of the gray level data sets provide a well-defined lattice with acceptable fidelity of the complex fibrous structure. The mass density variations formed from the different engineered features that may exist in these papers are well represented if the dimensions of the lattice elements are sufficiently small. This enables the model to respond to local gradations in density, irregularities in wettable surfaces and variation in interfiber spacing. The three phase system is represented within the 3D lattice, where the elements representing the fibrous structure are static and the fluid elements, liquid and air, are interchangeable depending on the cumulative interaction energies of the central element with the surrounding neighbors. The interfacial energies of the liquid and

fiber, in this case water and lignocellulosics, determine the extent to which the liquid advances within the structure. To implement the simulation, a seed region was populated with the liquid elements. While seed regions can be of any shape and located anywhere within the 3D lattice, in this study a small spherical region of liquid elements was placed in contact with fibers at the surface or within the structure. The simulation was then initiated so that each element at the liquid-void boundary was tested to determine if the energetics favored reassignment of that element. A single sweep of all elements at the liquid/void boundary constitutes one iteration. The process is repeated until the outer boundary of the entire data set was reached or the simulation was terminated.

Wetting Model Assumptions and Constraints

1. The fibrous structure is based on the dimensions of the XR-3DM data set. Model space is constrained in 3 dimensions by the data set.
2. The fibrous structure is stationary. Fibers do not swell or move in the model.
3. The model only considers three phases, solid, liquid and void; all are homogeneous.
4. Interaction energies are based on uniform surface chemistry. Water contains no dissolved species. Fiber surfaces contain no soluble components.
5. Only elements at the liquid/void boundary are tested to undergo a change based on minimization of the total interaction energy with the 18 contacting neighbors.
6. Liquid volume is not constrained (infinite reservoir) and increases as void elements are changed to liquid.
7. The model is not dynamic and has no time component. It assumes steady state at the liquid/void boundary at the end of each iteration. There is no memory of prior exchanges.
8. Global interaction energy of the liquid phase is not balanced.
9. Hydrodynamics are neglected. Viscous flow through the structure and along fiber surfaces is not considered.
10. Vapor deposition in advance of the liquid front is not considered.

The Wetting Model

Using the volumetric space generated by a three-dimensional imaging system, in this case 3D-XRM, the model space consists of a 3D Cartesian grid, *J*, of dimensions $N = X \times Y \times Z$. Experimental data was used to populate the space so that each element, $j \in J$, is identified as solid, liquid, or void. For this study, elements were occupied by fiber, water, and air, respectively. A phase identifier, ϕ, was used to identify the phase state so that:

$$\phi^L = 1; \quad \text{if the element is liquid}$$

$$\phi^S = 1; \quad \text{if the element is solid} \tag{1}$$

$$\phi^V = 1; \quad \text{if the element is void}$$

The central premise of this model is that through a series of iterations, each element at the liquid/void boundary is populated with a phase that minimizes the interaction energy, E, between that element and all neighboring elements, i, in direct contact with j. Thus, for each element, a total interaction energy, E, is calculated for the central element, j, as a liquid or void, and by comparison the lower energy determines the new phase. A liquid or void boundary element can remain the same or be reassigned to the other phase. At the end of an iteration, the liquid/void boundary generally changes significantly in response to the interactions of the two fluid phases with the stationary solid phase and each other. The iteration process was then repeated.

To simplify computation, the total number of elements of each of the three phases neighboring the element j were determined and these are multiplied times the appropriate interaction energy. Thus, the local density of the phases, liquid, L, solid, S, and void, V, in the nearest neighbors, i, surrounding voxel j are represented as

$$L_j^1 = \sum_{\substack{i \varepsilon J \\ p(j,i)=1}} \phi_i^L \quad S_j^1 = \sum_{\substack{i \varepsilon J \\ p(j,i)=1}} \phi_i^S \quad V_j^1 = \sum_{\substack{i \varepsilon J \\ p(j,i)=1}} \phi_i^V \tag{2}$$

The notation $p(j, i) = 1$ indicates that element i shares at least one plane in common. The total count of such first order neighbors is, $N_1 = 6$, cf. Figure 4. The current model also includes adjacent neighbors that share a common edge with element j using the notation, $\sigma(j, i) = 1$. In that case $N_1 = 12$, see Figure 4. Therefore, a total of 18 neighbors are included in each energy comparison. The terms in eq. 2 provides the total count of each of the three phases that are in contact with the central element, j.

Interaction energy between two elements, j and i, depends on the phase and chemical composition of each, values of which were obtained from the literature. Free energy change per unit area of contact, or reversible work done, can be adhesive, W_{SL}, if the two interacting elements are a liquid and a solid or cohesive, W_{LL}, when two liquid elements interact with each other. For the situation where one element is liquid and the other is void, then the surface tension of the liquid, γ_L, contributes to the total interaction energy. Likewise, if one element is solid and the other is void, then the interfacial energy of the solid, γ_{SV}, is used.

Work of cohesion between two liquid elements is defined as

$$W_{LL} = 2\gamma_L \qquad (3)$$

From the Young –Dupré equation, the work of adhesion between a liquid and solid, W_{SL} , is expressed as:

$$W_{SL} = \gamma_{SV} + \gamma_L - \gamma_{SL} = \gamma_L \, (1 + \cos\theta) \qquad (4)$$

Expressions for the summed energy contributions for neighbors of each of the three phases are given in eq. 5 when j is liquid and eq. 6 when j is a void space.

$$E_{LL,j} = -W_{LL}^1 L_j^1, \quad E_{LV,j} = -\gamma_L V_j^1 \quad E_{SL,j} = -W_{SL}^1 S_j^1 \qquad (5)$$

$$E_{VL,j} = -\gamma_L L_j^1, \quad E_{VV,j} = -\gamma_{VV} V_j^1 = 0 \quad E_{VS,j} = -\gamma_{SV} S_j^1 \qquad (6)$$

Since γ_{VV} is effectively zero, so too is $E_{VV,j}$, so that term will be dropped in subsequent equations. Summing the contributing three phase interaction energies under the conditions that j is either a liquid or solid, and by substituting local phase counts from eq. 2, the total interaction energies, $E(\phi_j)$, used for comparison are given in eq. 7 and 8.

Total interaction energy for j = liquid:

$$E(\phi_j^L) = -\sum\left(W_{LL}^1 \sum_{p(j,i)=1} \phi_i^L + \gamma_L \sum_{p(j,i)=1} \phi_i^V + W_{SL}^1 \sum_{p(j,i)} \phi_i^S \right) \qquad (7)$$

Total interaction energy for j = void:

$$E(\phi_j^V) = -\sum\left(\gamma_L \sum_{p(j,i)=1} \phi_i^L + \gamma_{SV} \sum_{p(j,i)=1} \phi_i^S \right) \qquad (8)$$

To include more distant neighbors, in this case those that share a common edge with j, the notation, $\sigma(j, i) = 1$ is used. For this situation, the interaction energies are reduced by $\sqrt 2$ to account for the geometric distance. The surface interaction terms are also substituted:

Interaction energy for j = liquid:

$$E(\phi_j^L) = -\sum \gamma_L \left(2 \sum_{p(j,i)=1} \phi_i^L + \sum_{p(j,i)=1} \phi_i^V + (1+\cos\theta) \sum_{p(j,i)=1} \phi_i^S \right)$$
$$- 0.7071 \sum \gamma_L \left(2 \sum_{\sigma(j,i)=1} \phi_i^L + \sum_{\sigma(j,i)=1} \phi_i^V + (1+\cos\theta) \sum_{\sigma(j,i)=1} \phi_i^S \right) \qquad (9)$$

Interaction energy for j = void:

$$E(\phi_j^V) = -\sum\left(\gamma_L \sum_{p(j,i)=1} \phi_i^L + \gamma_{SV} \sum_{p(j,i)=1} \phi_i^S\right)$$
$$-0.7071\sum\left(\gamma_L \sum_{\sigma(j,i)=1} \phi_i^L + \gamma_{SV} \sum_{\sigma(j,i)=1} \phi_i^S\right) \quad (10)$$

For a single iteration, the energy values $E(\phi^V)$ and $E(\phi^L)$ are compared for all elements, j, at the liquid/void interface. Element j will take on the phase for whichever interaction energy is lower, so that:

$$E(\phi_j^V) < E(\phi_j^L) \quad \text{then} \quad \phi_j^V = 1, \quad \text{element } j \text{ is assigned as a void space}$$
$$E(\phi_j^V) > E(\phi_j^L) \quad \text{then} \quad \phi_j^L = 1 \quad \text{element } j \text{ is assigned as a liquid} \quad (11)$$

This completes the testing of a single element in the data set. Each element in the sampled region is tested to determine if it is liquid or void, and if so, whether it is at the liquid/void interface. If both are true, then the total interfacial energy comparison performed in eq. 13 is repeated for that element. A single iteration is complete when all elements in the sampled region have been tested.

EXPERIMENTAL

Materials

Paper towels samples examined in this study were retail kitchen towels sold in the U.S. and selected to represent a wide range of structural properties. Samples selected as a broad cross section of retail products are identified in Table 2. Those samples identified as conventional wet pressed (CWP), also referred to as light dry creped, have structural features induced by Yankee creping and the embossing process [7]. Samples identified as TAD and ATMOS are referred to as structured tissues, and have more complex structures developed by wet contour forming in addition to creping and embossing. Table 3 identifies three samples of the same commercial product manufactured using the same methods but composed of different fiber furnishes. Sample CWP-3A was made using secondary/recycled pulp. CWP-3B was made using virgin kraft pulp fibers. CWP-3C was made using sawdust kraft pulp fibers.

All samples used in this study were two-ply products. The plies were carefully separated and the outer ply, i.e. the external ply on a converted roll, was used in

Table 2 Paper towel samples from various manufacturing processes tested in this study

	Grammage T410 (g/m^2)	Process
TAD-1	27.4	Through Air Dried
TAD-2	30.4	Through Air Dried
ATMOS	24.7	ATMOS
CWP-1	24.6	Conventional Wet Pressed
CWP-2	20.9	Conventional Wet Pressed

Table 3 Paper towel samples from various manufacturing processes tested in this study

ID	Grammage T410 (g/m^2)	Furnish
CWP-3A	25.5	Secondary/Recycled
CWP-3B	23.9	Virgin kraft
CWP-3C	24.5	Sawdust kraft

all testing. Samples were preconditioned and tested under TAPPI standard conditions of 50%RH, 23°C [67]. Tables 2 and 3 provide value for gravimetric grammage using T410 [68].

2D Imaging Methods

Structural characterization was performed using 2D and 3D X-radiographic methods to determine the spatial distribution of fibrous mass within the samples. Soft X-radiographic imaging was combined with non-contacting twin laser profilometry (TLP) to map the inplane thickness, apparent density and out-of-plane deformation in areas of sufficient size for the analysis of micro wetting experimental results. XR-3D microscopy was used to obtain data sets representative of the 3- dimensional structure needed for numerical simulation studies.

Grammage Maps Using Soft X-Radiographic Imaging

Two-dimensional grammage maps were obtained for all samples using the soft X-radiographic imaging method previously described by Keller *et al.* [69, 70]. Keller and Pawlak [71] demonstrated that edge definition is lost as a function of distance from the detector when using a diffuse source. Traditional contact β-radiography [71–73] is therefore an unsuitable method for capturing formation maps for tissue and towel papers that generally have large thicknesses due to creping and embossments. X-radiography uses a point sourced that provides a

much larger depth of field giving clearer edge definition and higher resolution throughout the entire thickness of samples. A Minishot X-Ray cabinet (Associated X-Ray Corporation East Haven, CT) was used to generate a 6 kV and 4.5 mA conical beam of low energy (soft) X-ray. Samples were held in a restraining frame that exposed an 80×80 mm^2 region of the specimen. The frame also held a step wedge with five thicknesses of Mylar for use as an internal grammage calibration reference. X-ray film (Structurix D2, Agfa) was placed beneath the restraining frame to capture transmitted radiation. The inplane distribution of mass was determined based on the method developed by Feng *et al.* [69, 74]. Gray level images were obtained after optical scanning of the developed film at a resolution of 4800 dpi producing a practical resolution of ~10 μm considering all aspects of the radiographic process. Images were corrected for vignetting distortion attributed to the exposure geometry and converted to 16-bit grammage maps using the calibration reference [74].

Thickness Maps Using Twin Laser Profilometry (TLP)

Thickness mapping was performed using the twin laser profilometry (TLP) method introduced by Sung *et al.* [75]. That method uses the simultaneous range measurement of opposing sides of the sample using non-contacting laser triangulation. Precision of the method was shown to be 1 μm in three dimensions. For paper towel samples with low density, a discontinuous external surface, and often with protruding fibers, TLP maps can have a significant amount (>10%) invalid data points [76]. For this reason, samples were mapped with an inplane spacing of 50 μm. Thickness values were used for calculation of local apparent volumetric density.

Apparent Density and Center Surface Maps

The local apparent volumetric density maps were produced by reducing each element of the grammage maps from soft X-radiography with the corresponding element of TLP thickness maps to yield local density in units of g·cm^{-3}. The TLP technique also generated center surface maps indicative of the out-of-plane deformation of the sample.

3D Imaging Methods

X-Ray 3D microscopy

The suitability of contemporary XR-3D microscopes for providing resolution to analyze the structure of towel and tissue papers was demonstrated by Keller

D. S. Keller, H. Abedsoltan, J. Reid and L. Yin

et al. [70, 77]. High resolution XR-3DM was used to obtain representative data sets for use in the wetting simulation. The same data sets were also used to generate 3D local density maps. From local density, the effect of pore space and fiber separation on the tendency for liquid to advance through the structure was examined. XR-3DM imaging was conducted at the Imaging Technology Group, Beckman Institute at the University of Illinois using an Xradia Bio MicroCT (MicroXCT-400, Carl Zeiss Microscopy). Samples were mounted onto a frame made of a thin plastic sheet (~200 μm thick) with a rectangular aperture slightly larger than the field of view. Paper samples were attached to the frame by double-sided tape that kept samples flat without straining. Projections were generated using X-ray energy of 40kV for an exposure time of 10s. A total of 951 projections were taken for 190° scan angle. The data sets generated by radon transform had an element size of 2.5 μm and imaged regions of 2000 × 2000 elements (5 × 5 mm^2) in stacks of slices (~350) spaced 2.5 μm apart. The data sets were saved as 16-bit gray scale TIF files. Each data set was cropped to eliminate extraneous void regions in each dimension. The resolution of the tomographic data sets and the segmentation process used to distinguish the solid and void elements are crucial for obtaining representative results from the wetting simulation. Segmentation was performed using a routine executed in the Avizo application. Auto-thresholding by factorization based on the Otsu criterion using 3D interpolation provided data sets with sufficient resolution and noise filtering for the purposes of this study. Other more elaborate segmentation methods were tested and found to have little effect on the results produced by the simulation. Data sets were binaraized to remove gradation at fiber edges. Three dimensional representations of the tomographic data sets were generated using the Avizo software. Data are also represented in two dimensions by summing in the Z-direction that is perpendicular to the principal X–Y plane of the fibrous structure.

Apparent Density and Center Surface Maps

Local density maps were determined from XR-3D microscopy data sets in order to examine the influence of through structure density, i.e. void space, on the local movement of liquid. The procedure, previously described by Keller *et al.* [70], involved the generation of two surfaces representative of the external surfaces of the sample by connecting Z extrema points at each in-plane position. Smoothing using a 3D moving average algorithm attenuated extraneous protruding fibers. Void spaces were filled and smoothed using a windowed transform function. The center surface was determined by difference between the upper and lower surfaces for each inplane position. Figure 5A illustrates the sectioned projection in the X–Z plane of the outer ply of a two-ply TAD towel. The profiles of the upper, center and lower surfaces are shown. The bottom image in Figure 5B shows the
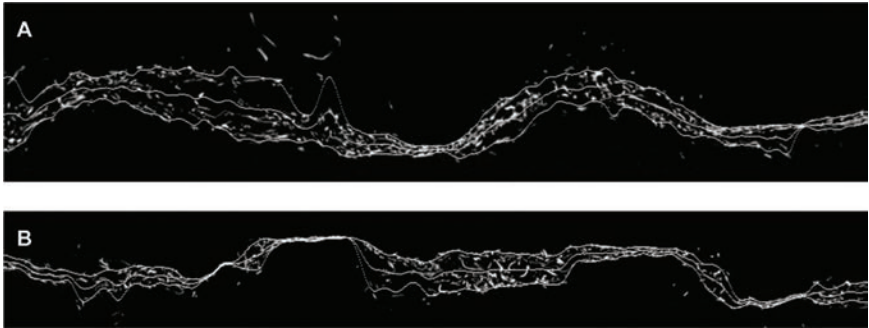
Figure 5. Sections in the X-Z plane of two different TAD samples taken from XR-3DM data sets. In both cases the two external surfaces were calculated from the extreme upper and lower Z values at each in-plane position. The extrema surfaces were smoothed and the center surface determined as the mid-point between the two [70].

three profiles for a different TAD towel. Note the bulked and densified regions and the dampened response to fibers that extend from the surfaces. Three-dimensional height color map representations of the center surface maps for two TAD samples are shown in Figure 6. Figure 6A shows an example of one ply of a towel that is compressed around the base of circular TAD features that protrude upward from the base. The towel shown in Figure 6B was compressed within the TAD features so that the periphery remains bulky, presumably for increased absorbent capacity.

Local thickness values are determined along the surface normal vectors of the center surface, Z', at regular in- plane intervals, as shown in Figure 7. Thickness is calculated as the length of the line segment between the external surfaces. Note that the surface normal vector, Z', will also have angular components in the ZY and ZX planes. By this method the structural thickness of materials with prominent features, such as TAD or embossing patterns, can be accurately determined.

Local apparent density is calculated using the thickness measured along the surface normal vectors, Z', derived from the center surface map. The element count along the line segment between the upper and lower surfaces represents mass and the line segment length indicates local thickness, cf. Figure 7. Apparent density is plotted at regular grid intervals within an arbitrary X–Y plane that is closely aligned with the principal plane of the sample. Figure 6C,D, shows XR-μCT projections with color maps representing apparent density projected onto the center surface, cf. Figure 6A,B, for the same two TAD towel samples. Densified regions are mechanically strengthened by interfiber bonding. The bulked regions act to impart flexibility and absorption capacity.
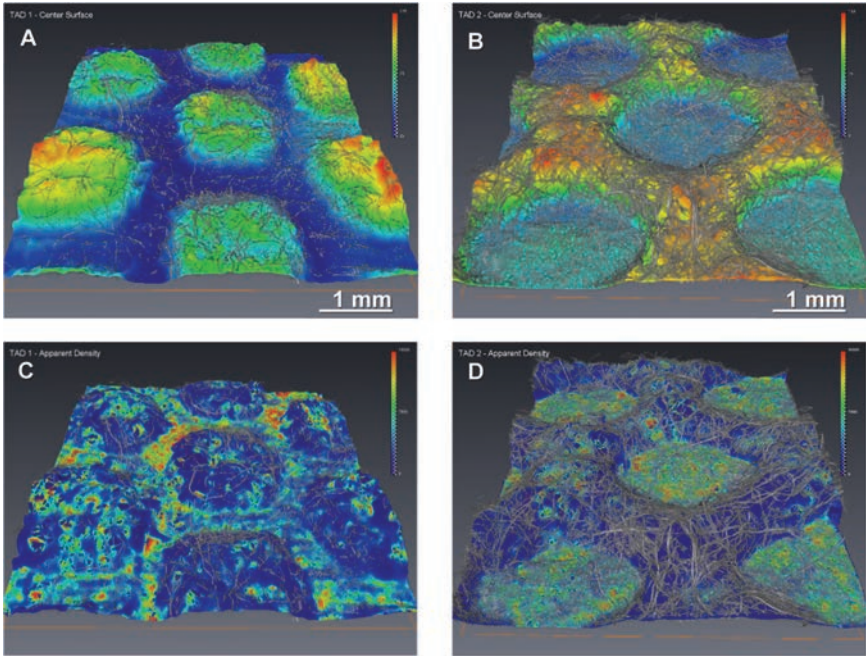
Figure 6. Maps of the center surface (A and B), and apparent density (C and D), of two TAD towel papers calculated from XR-3DM tomographic data. [70]
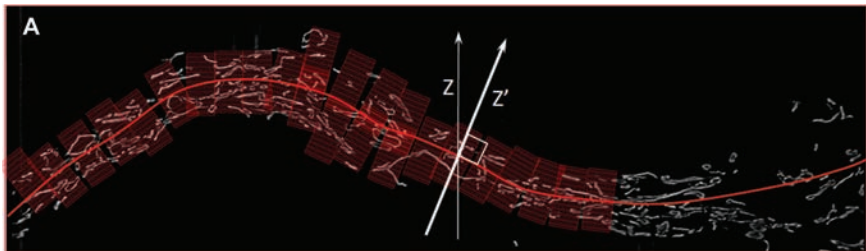
Figure 7. Calculation of thickness and apparent density from XR-3DM data. Thickness is determined from the length of a segment along the surface normal line, Z', that extends between the two external surfaces passing through the test point. Apparent density is calculated using the solid element count, i.e. mass, along the line segment.[70]

Liquid Absorption Testing

Wetting experiments were conducted by injecting small volumes of probe liquid (water) into a point near the sample center and then recording the liquid movement at fixed interval times. The experimental design was similar to other hori-

zontal radial spreading tests, such as GATS or CRT discussed above, although the delivery volume was much lower and the rate of injection was controlled. Also, the imaging system provided much greater spatial resolution that revealed finer details of the liquid movement through features and fibrous flocs. By injecting a fixed volume at a controlled rate, the source is considered a flow constrained infinite reservoir to that point at which the full volume of liquid is delivered. After that, the liquid continues to spread by capillary forces from what is considered a finite reservoir. In earlier work by Keller and Abedsoltan [78–80], an infrared camera was shown to provide excellent definition between the wet and dry regions when the probe liquid is water. Image frames were analyzed to quantify the wetted area and the position of the bounding perimeter from which an approximation of the local rate of wetting and other characteristic parameters were determined.

IR µ-Wetting Apparatus

The IR µ-wetting apparatus developed in an earlier study [78] is illustrated in Figure 8. The specimen is held horizontally between two restraining disks, each having a 25.4 mm circular opening in the center. Thus, the sample was accessible on the upper side for injection of the liquid using a micro syringe and on the lower side where the sample was imaged. An UltraMicroPump, UMP3 (World
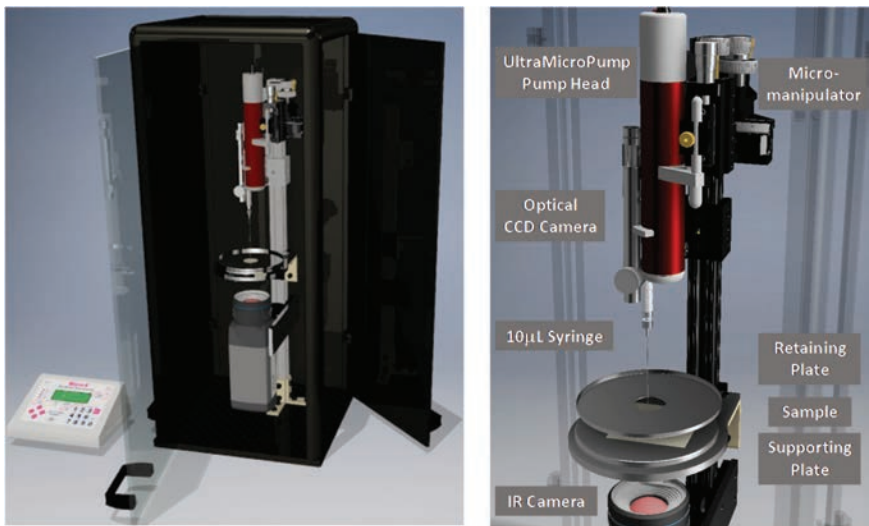
Figure 8. Illustration of the micro-wetting apparatus. The micro-syringe pump is shown in red. The Infrared camera is affixed along the same axis viewing the sample upward. The sample is held between two plates that expose a 25.4 mm circular region in the center.
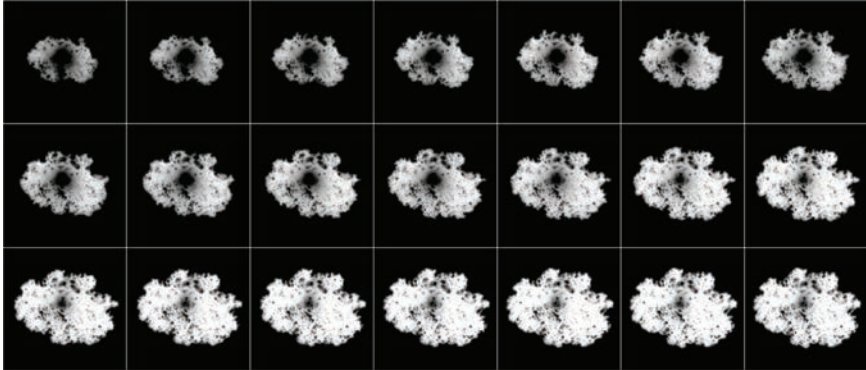
Figure 9. A sequence of infrared images captured during a μ-wetting test of a TAD paper towel. Images shown here at 3 second intervals.

Precision Instruments LLC) micro syringe pump fitted with a 700 series micro-liter syringe (Hamilton Company) was used to deliver small volumes of liquid to the samples. Generally, a 10 μL or 25 μL syringe was used. The syringe pump was attached to a manual micromanipulator that enabled 3-axis positioning for precise placement of the syringe tip with respect to the sample. A T-slotted rail system assembly was used to rigidly align the micromanipulator, sample stage and imaging camera. The instrument was fully enclosed to control temperature, humidity and to isolate from air currents and ambient infrared radiation.

Images were captured using a research grade longwave infrared camera (A655sc, FLIR Systems Inc.) equipped with a close-up IR lens (2.9x). This camera had a microbolometer sensor with 16-bit gray level sensitivity and a spatial resolution of 640 x 480 pixels. Contrast between wet and dry regions was based on the temperature difference, where under TAPPI standard conditions [67] the wet-bulb temperature depression is 6.5 °C [81]. The wet–dry boundary was resolved to a resolution of ~50 μm as aqueous solutions were injected into fibrous samples. Imaging sequences were collected at 6 Hz for data set sizes up to 700 images using the ResearchIR-64 (FLIR Systems Inc.) system software. Images were exported in 8-bit TIFF file format for subsequent analysis. An example sequence of images taken at 3 second intervals is shown in Figure 9. Notice that an artifact forms at the injection site, visible as a dark region near the center of the wet region. This was masked during analysis for measurement of wetted area.

IR μ-Wetting Experiments

For wetting experiments, the sample was held between the restraining disks and the syringe needle was positioned in the center of the exposed test region, cf.

Figure 8. Prior to testing, an infrared source was used to capture a transmitted image that revealed structural patterns that were used for registering images with grammage, thickness and apparent density maps in the analysis. The liquid was delivered at a preset rate using the micro syringe pump equipped with a 10 μL syringe. A test series involved injecting a fixed volume of probe liquid, in this case 2μL at a fixed injection rate. Separated tests were conducted using injection rates of 50, 100, 200, and 400 nL/s.

The dynamic response was measured by the change in area and the wet/dry boundary up to the point where the total volume was injected (infinite reservoir) which nominally spanned from 5 to 25 seconds. Thereafter, the liquid continued spreading for an additional 120 to 180 seconds due to capillary forces.

IR μ-Wetting Analysis

Three aspects of dynamic wetting were considered for towel samples. The inplane spreading rate was determined using the expansion of the wetted area with time. This analysis bears similarity to other horizontal radial wetting experiments, although in this case and for that previously reported by Abedsoltan *et al.* [78–80], the injected volumes were much smaller. The second aspect was determination of the instantaneous local spreading velocity as a function of inplane position for the infinite and finite reservoir wetting regimes. This analysis sought to observe the effects of web structure on local spreading direction, and to quantify the rate that the front advanced, independent of direction. The third analysis involved alignment of local spreading velocity with local structural maps for the same region to examine the extent of correlation.

The wet/dry boundary was determined for each image in the injection test series. A relative threshold that varied based on the unique intensity distribution of each image was set, and wet and dry regions were identified. Custom routines (scripts) were written in MATLAB. Wetted area, A_{wet}, was taken to be the entire region within the wet/dry perimeter, as shown in Figure 10. In some cases, the wetted region contained spaces where the liquid was not present, A_{void}, as the result of pin holes of sufficient size where the liquid was unable to advance to fill the void.

The local spreading velocities, v_x, for each point, $p_x(t)$, along the perimeter curve, $P(t)$, were determined by measuring the distance that the wetted region expanded between a fixed time interval, i.

Expansion was calculated for each point on the perimeter by first determining the tangent vector from a windowed region surrounding the point, which in this case had dimensions of 25 × 25 elements, as illustrated in Figure 11 (left). The normal vector was then calculated. The length of a line segment along the normal vector between $p_x(t)$ and the perimeter at the next time interval, $p(t + i)$, was used to calculate local velocity, v_x as shown in Figure 11 (right). In this study, the time interval used to calculate v_x was 0.5s < i < 4s.
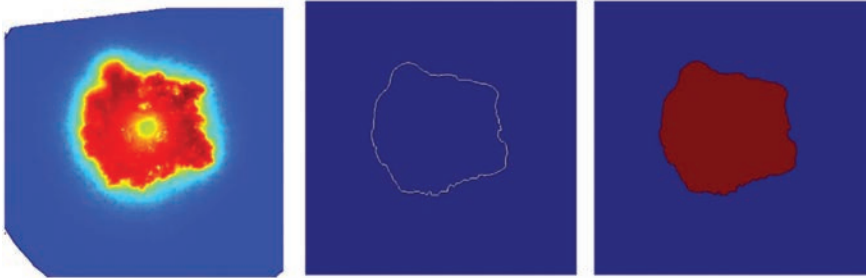
Figure 10. Examples of the image processing. At left, an image captured from the IR Camera showing the wet/dry boundary as yellow. The center shows the perimeter, and right shows the area calculated for each captured image.
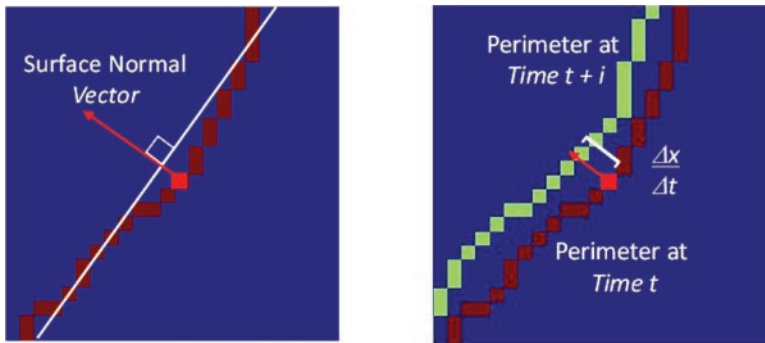
Figure 11. Diagrams illustrating the method for determining the velocity gradient for the advancing wet/dry boundary in μ-wetting experiments. At left is shown how windowed points on the perimeter are used to determine the normal vector. The right picture shows how the length of the line segment between perimeter and the perimeter after a given interval, *i*, was used to determine local velocity.

ANALYSIS

The foremost aim of this investigation was to provide accessible tools to characterize the wetting behavior of paper towels using experimental observation and by numerical modeling using XR3DM representations of the structure. The fidelity of the model used to simulate wetting was validated by comparison with results from wetting experiments. A second goal was to demonstrate the use of these methods to compare the wetting of a variety of retail towel samples that have distinctively different structural features. The flowchart shown in Figure 12 illustrates the steps taken for experimental and simulation methods used in this study.
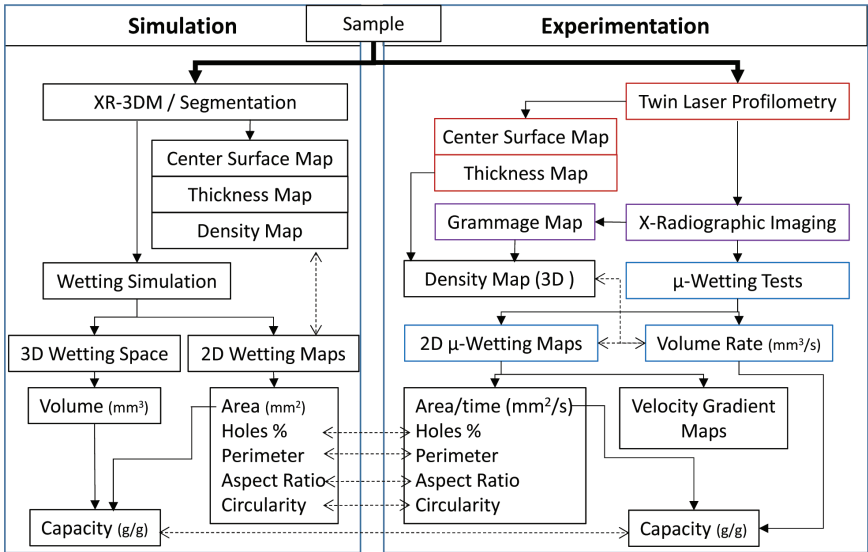
Figure 12. Flow diagram of the steps taken for the comparison of the results from the model simulation with those from the experimental.

Each step, connected by solid lines, will be described thoroughly in the Results section. Comparisons between descriptors derived from simulated and experimental images and data sets are shown using dashed lines.

RESULTS: μ-WETTING EXPERIMENT

Comparison of Forming Methods

The first test series involved a comparison of samples representing the TAD, ATMOS, and CWP forming methods. Figure 13 illustrates the structural maps for the three samples. The left column shows the X-radiographic grammage map. The point source geometry of the incident beam provides inplane resolution below 25 μm through the entire web. This also has the effect of highlighting vertical surfaces, such as the side walls of embossments. Fabric patterning is clearly visible in the CWP sample, as well as a coarse, deep pattern in the ATMOS sample. Thickness maps are provided in the right column in Figure 13 where the differences between the samples are more apparent. The TAD sample shows the clear pattern of densified oval features surrounded by a continuous bulked region.
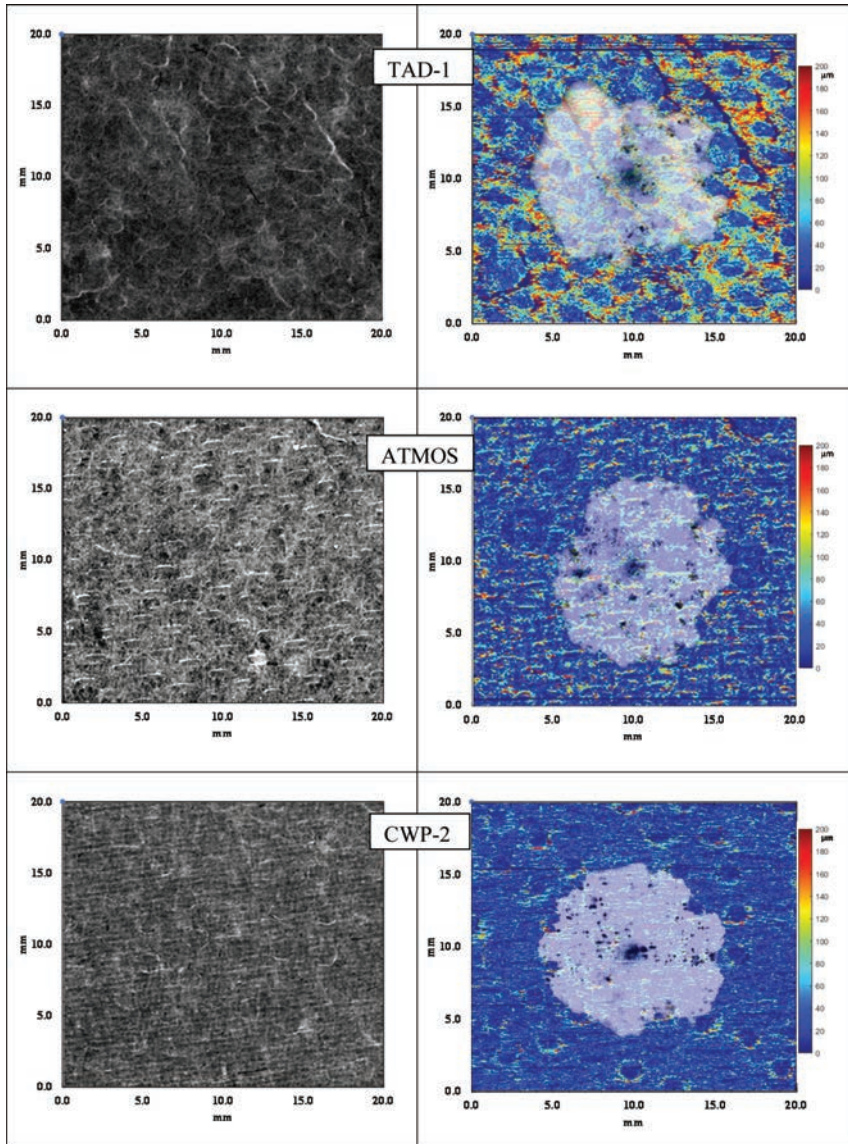
Figure 13. Structural maps for three outer-ply towel samples showing the same region that μ-wetting tests were performed. The left column shows the grammage maps obtained from X-radiographic imaging. The right column shows thickness maps obtained from twin laser profilometry. Actual wetting images captured at the maximum wetted area after the injection of 2 μL of water.

The difference in thickness approaches 100 μm in some cases. Close inspection reveals a subtle creping pattern. The ATMOS sample also shows contrasting thickness values, specifically at knuckle contact points in the cross-machine direction. Compression at the embossments is also clearly shown. The CWP sample also shows compression at the embossments in what is otherwise a relatively uniform thickness map. While the fabric pattern is not as dominant as in the grammage map, crepe lines are detected in this sample. Density maps were calculated, however the results provided little additional insight.

A complete series of wetting injections was performed on the three samples. In each case, the wetted area, A_{wet}, expanded linearly during the injection (infinite reservoir) and slowed after the total volume was delivered (finite reservoir). Wetted area approached an asymptotic limit, A_{max}, consistent with the results previously reported by Abedsoltan [78, 79] for the same samples. Of interest in this study was the relationship between wetting and the structural features. In Figure 13, the image of the wetted region when A_{max} was reached is overlaid and aligned with the thickness maps. For each sample, spreading appeared to slow at the embossments, where the web is thinnest.

Non-Wetted Regions

The wetted region of each sample had submillimeter vacancies or "holes" where the water did not wet or was wicked away from by capillary forces. The presence of these non-wetted regions was observed using transmission light microscopy in an earlier study [80]. Non-wetting appears to occur when interfiber spacing is sufficiently large to prevent liquid bridging. Just prior to injection tests, IR backlit images were acquired. Examples of these images for the three samples are shown in Figure 14(left) where the void spaces are shown in white. The dark spot in the center indicates the cooling effect of the needle that is in contact with the upper surface. The results for infrared imaging are shown in the center column of the same figure. Images were selected from the series where the wetted area, A_{max}, is at a maximum. Image contrast has been enhanced to improve the definition of the wet/dry boundary. Part of the wetted region appears defocused. This changes during the test and appears to result from localized out of plane buckling that moves the region out of the focal plane of the camera. Three morphological differences are apparent when these images are compared. First, the areal coverage differs, with the wetted region of the TAD sample appearing to occupy smaller area, thereby having a greater volume per area than the ATMOS and CWP samples. Secondly, the spot shape shows differences in circularity, aspect ratio and orientation. The preferential cross machine direction orientation of wetted spots has been noted by other investigators [26, 28] and attributed to tracking of water along the creping lines. The extent to which structural features are present
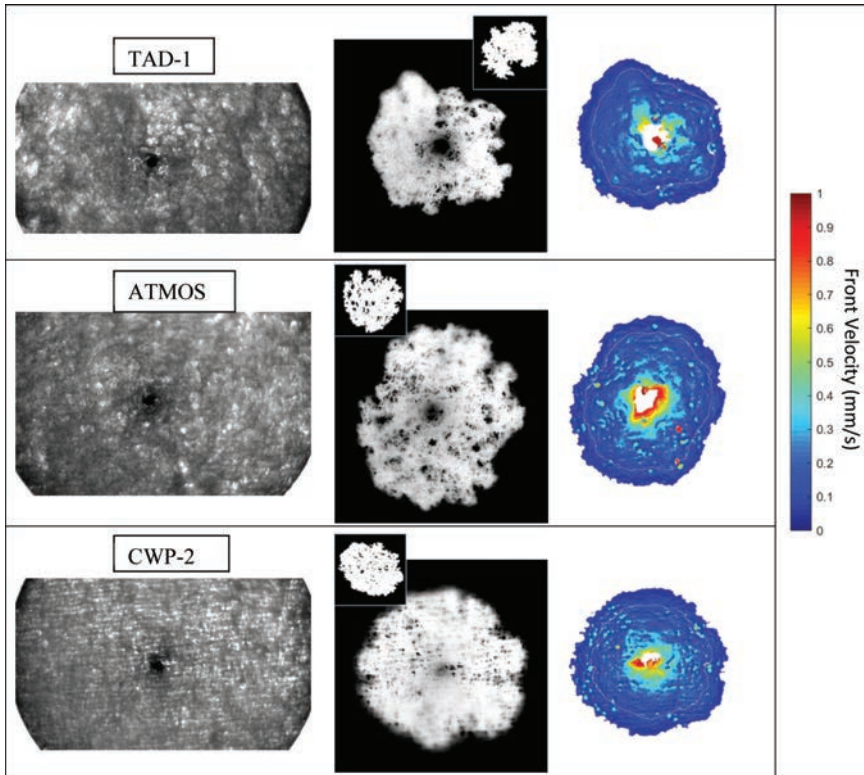
Figure 14. Images from the µ-wetting experiments performed on three paper towel samples. The left column shows images captered by the IR camera with infrared backlighting to show the structure in transmitted illumination. The center column shows the contrast adjusted wetted region captured at the maximum wetted area after the injection of 2 µL of water. The right column illustrates the local spreading velocity taken from each point along the perimeter for the duration of the test. Sampling interval was 6s. The white perimeter defines the time when the entire volume was delivered and capillary spreading takes over.

disrupts the uniformity of radial flow. Lastly, the occurrence of non-wetted areas appears related to, but not fully dependent on void spaces in the sample. It is expected that non-wetted spaces will depend on 3-dimensional interfiber spacing which is not fully represented in these 2D projections. The insets that are shown with the infrared images in Figure 14 (center) were generated using the wetting simulation and are at the same length scale. These are provided to demonstrate how the simulation generates 2-D images with morphologies that appear similar to those acquired from the µ-wetting tests.

Dynamic Local Wetting Velocity

The velocity of the wet/dry boundary as the liquid was injected then permitted to continue spreading was determined for each of the three samples. Figure 14 illustrates the change in velocity with time as determined using 1 second intervals (6 frames). Velocities near the center of the plot are not shown since the flow during the first few seconds is subject to turbulence as the liquid is discharge from the needle. Channels where flow velocity is greater can be seen in the TAD sample and to a lesser extent in the other samples.

Flow velocity was influenced by finer structural features such as fabric patterns and holes. The time at which the full 2 μL volume was delivered, marking the transition between infinite and finite reservoir wetting, is shown by the white line just inside the outer perimeter. The flow behavior does not appear to change significantly at this transition. Generally, flow is <0.4 mm/s for the three samples.

Comparison of Fiber Furnish

A second test series was performed to compare the effects of fiber furnish on the wetting of towels made using the same forming process and to the same specification. The conventional towel samples CWP-3A, B and C use pulps from secondary/recycled, virgin kraft and sawdust kraft, respectively. Infrared images taken when the wetted area first reaches the maximum value, A_{max}, are shown in Figure 15. Once again the morphological differences are evident. Sample CWP-3B, with larger kraft fibers shows a more open structure, with larger void spaces and the local wetting velocity appears more irregular than for the other two samples. Embossments appear to obstruct the flow of all samples, although in non-embossed regions the curvature of radial flow is apparent. Sample CWP-3A, composed of secondary fibers, appears to have the most uniform distribution of liquid with fewer void spaces. The flow velocity maps between CWP-3A and C were not significantly different. The local wetting velocity for these samples was in general <0.3 mm/s.

WETTING SIMULATION

Implementation of the Simulation

The numerical simulation for the wetting model used a brute force computational algorithm that tested the energetic state of elements at the liquid-void interface and performed phase reassignment to minimize energy. The simulation was coded in MATLAB 2020 (Mathworks) in the MS Windows 10 operating system. A single iteration of the test cycle consisted of the following. Each liquid or void
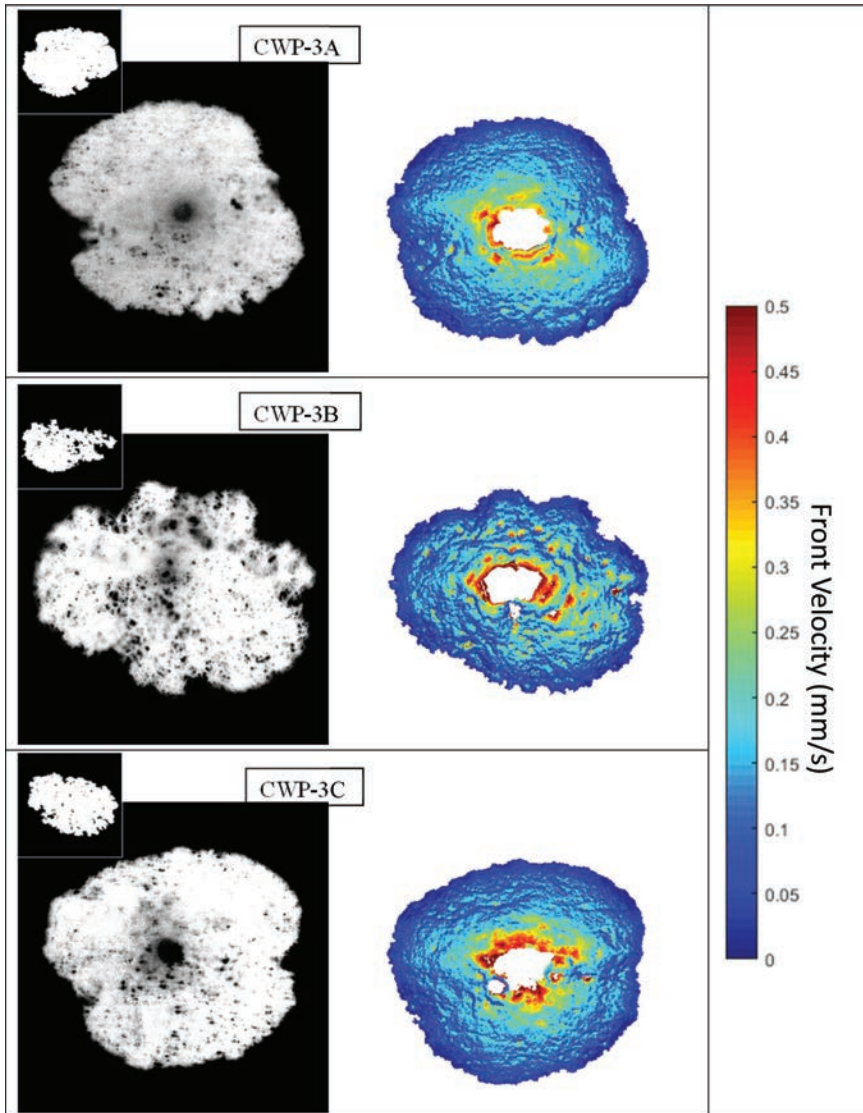
Figure 15. Images from the µ-wetting experiments performed on three paper towel samples formed from different fiber furnishes. The left column shows the contrast adjusted wetted region captured at the maximum wetted area after the injection of 2 µL of water. The right column illustrates the local spreading velocity taken from each point along the perimeter for the duration of the test. Sampling interval was 6s.

element within the array space was tested to determine if it was at the water/air boundary. If so, then for the center element the phase state of its nearest neighbors, in this case 18, were summed and multiplied by the respective interaction energies with either air or water. The phase of the center element was set to the phase providing the lowest summed interaction energy. With each iteration, an undefined number of elements had phase replacement, either from air to water or vice versa, effectively redefining the wet/dry boundary. Furthermore, as the wetted region expands, the number of elements at the interface increases quadratically, depending on the wetting response to the fibrous structure where wicking or the bypassing of regions occurs.

For a typical tomographic dataset in this investigation, 1.4×10^9 elements needed to be tested in each iteration cycle. Furthermore, energetic testing occurred for an ever-increasing subset of elements, an example of which is shown in Figure 16. Computational efficiency was improved by implementing two strategies. First, because of the expansive amount of computation and memory required to complete a simulation of useful size, the code was adapted so that the single element nearest neighbor problem could be solved by parallel processing. Multiple cores were used to solve the energetic calculations simultaneously. In the present study, the use of 16 of 18 cores reduced computation time by an order of magnitude. The parallelization was accomplished using a Single Program Multiple Data (SPMD) model. This required 2D vectorization of the 3D space. For each core, separate vectors were created and rotated appropriately for each of the 18 nearest neighbors. A second strategy for reducing computational time involved windowing the test region in the X–Y plane to reduce the total number of elements tested during each
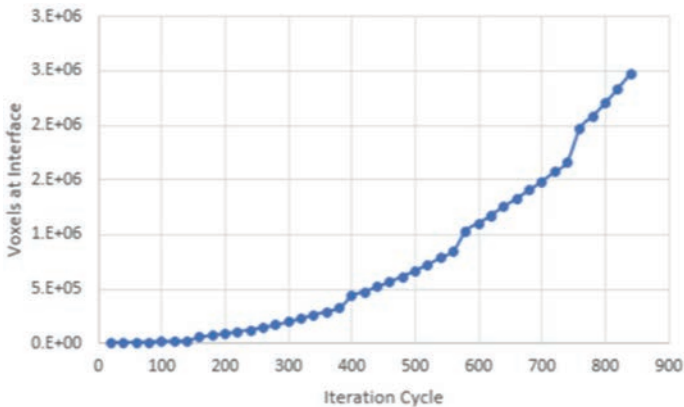

Figure 16. Number of liquid elements at the liquid/void interface as a function of iteration cycle for a typical XR3D data set used in this study.

iteration of the simulation. When the wetted region reached the boundary of the sub region, the window was enlarged and as a result the time to complete an iteration increased. By this method, calculation time was reduced to less than one third what it would have been without windowing. Computation was performed on a Lambda Dual (Lambda Labs, San Francisco), 3.00 GHz /i9/18 core CPU, 256 GB on board, Quadro RTX 8000 GPU. XR-3DM data segmentation and imaging processing were performed using Avizo (Thermo Fisher Scientific) software.

Simulations were initiated after placing a seed sphere with diameter of 50 elements or 125 µm near the center of the principal plane in contact with the fibrous structure. 3D data sets representing the space occupied by liquid elements were saved after every 20 iterations. 2D projections were also saved for later analysis and comparison with 2D images obtained from µ-wetting experiments. An example of a series of 2D images extracted from a full series is shown in Figure 17. The simulation was run until the external boundary of the data set was reached, which consisted of 2000 to 3500 iterations, depending on the sample thickness. Figure 18 illustrates a typical perspective view representation of the 5x5 mm^2 fiber structure (white) and water (blue). This example shows the expansion of the water phase in the first saved data set after 20 iterations. Notice how the seed has expanded and conformed to the void space that surrounds the fibers.

Simulation Parameters

Operational parameters for the simulation, including the data capture interval, the sub image increments and the surface energetic parameters were the only ones required for the simulation to run. In this study, all parameters were kept the same throughout the study. The parameters are provided in Table 4. All XR3DM tomographic imaging was performed on all samples at a 2.5 µm element size in a in 5× 5 mm^2 inplane space.
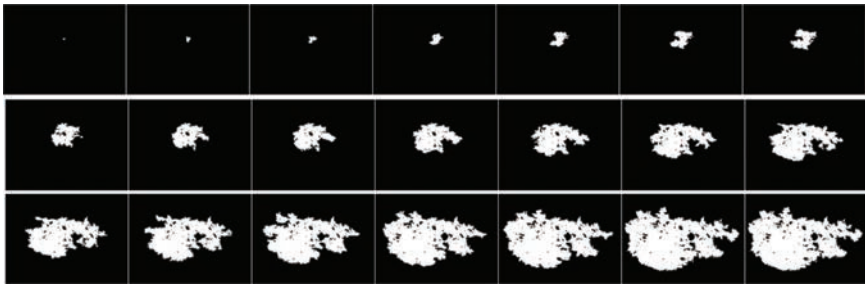
Figure 17. A series of 2D projections of the wetted region of a CWP towel generated by the simulated wetting within XR3D tomographic data. Images shown are every fith sample taken from the series.

Table 4 Operation parameters used in the simulation

|		
Surface Tension of Water (mJ/m^2)	γ_L	72
Surface Energy of Fibers (mJ/m^2)	γ_{SV}	52
Contact angle of Water on Fibers, (°)	θ	20
Image Capture Interval	i	20
Sub-image Windowing Increments		18
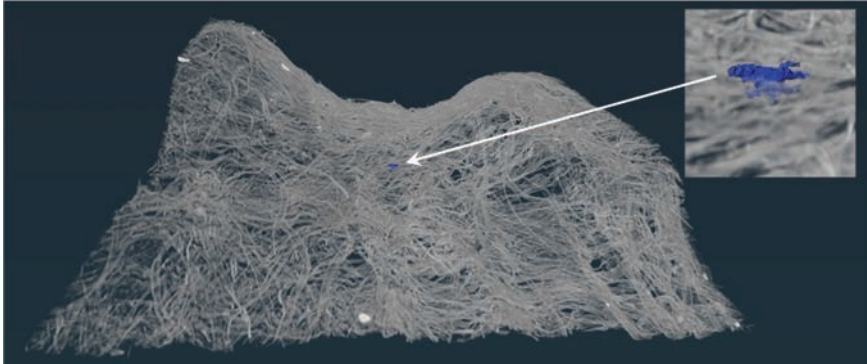
Figure 18. A representation of a typical XR3D tomographic data set used. Inset points to a seed location of the water phase data set generated by the wetting simulation after 20 iterations.

RESULTS: WETTING SIMULATION

Comparison of Forming Methods

Simulations were run on tomographic data sets acquired from two TAD, two CWP and one ATMOS towel samples. Representations of these are shown in the first column of Figure 19. For this study, embossed regions were included in all samples and in some cases constituted a significant amount of the inplane area. At this magnification, the differences in fiber morphology can be clearly seen. For example, the fibers in TAD-2 appear wider than those in TAD-1 and with closer interfiber spacing. Creping lines are observable in the two CWP samples. ATMOS and CWP-2 appear to have more through holes.

In the center column of Figure 19, the simulated water phase of the final iteration is superimposed on the fiber phase. The third column shows a magnification of the water phase only. One can gain a sense of how the model responds to out-of-plane features and the interfiber spacing from these projections. Gravitational forces are considered negligible in this model, since the volumes of the pixels are
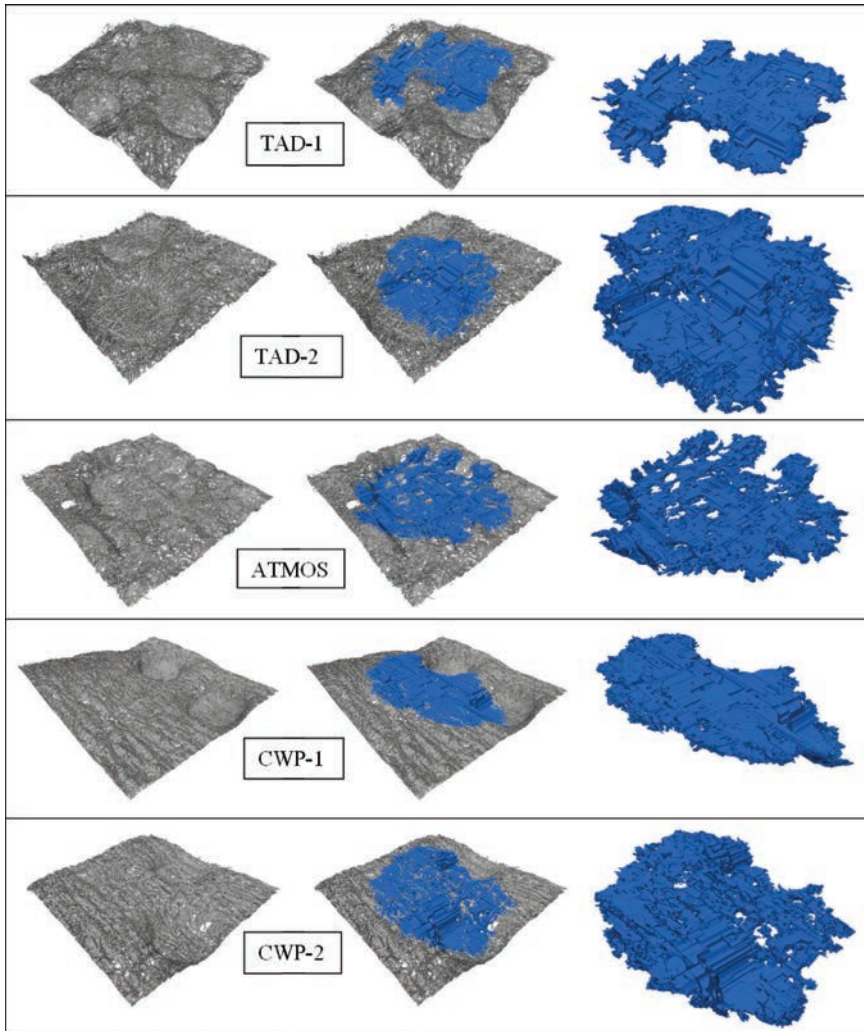
Figure 19. Representations of XR3DM data sets and respective water phase data gener-ated using the wetting simulation for towel samples from various processes. Imaged area is 5 x 5 mm^2 to a resolution of 2.5 µm. Left colum shows tomographs of fibrous structures. Center column shows fiber and water structures together. Right column shows a magnifica-tion of the water phase data.

so small, i.e. 10^{-9} g, and spreading occurs within the plane that is perpendicular to the gravitational vector. One may also notice that the liquid spreads along fibers, within the fiber lumen, and is especially promoted in the crevasses that form between aligned fibers. Simultaneous contact of the wetted region with multiple surfaces encourages wetting, as the surface tension forces of the liquid act in opposition. If the interfiber spacing is too large in a given region, so that the water phase cannot bridge the gap with the result that the region is circumvented. Liquid may approach the space from a different angle so that the space may then fill or remain vacant. Samples TAD-1 and ATMOS clearly show regions that are not infiltrated by the liquid. This causes the wet boundary to be more irregular. In the case of the ATMOS, the fiber structure appears to create a higher concentration of non-wetted spaces within the wetted region. Creping lines appear to have a significant effect on the aspect ratio and orientation of the wetted region, as the liquid phase in the CWP samples spreads more readily in the cross machine direction.

Faceted Surface of the Liquid Phase

The faceted appearance of simulated water phase is visible when magnified. Steps and squared corners appear where the surface of the water phase has expanded. Three aspects of the model contribute to this effect. First, global energy minimization is not performed on the surface of the liquid phase once the contacting contour is established. All energy evaluation is limited to the immediately neighboring region of elements at the liquid/void boundary. This might be addressed in future studies by the introduction of a step in the simulation that performs a zero sum global energy balance after a specified number of spreading iterations have occurred. Secondly, the simulation is conducted in a 3D Cartesian space, see Figure 4, where the degrees of freedom for liquid spreading is limited. Lastly, the resolution of the tomographic data set at 2.5 µm is about one-tenth of the fiber width and just less than the collapsed fiber thickness. Therefore, all of the tortuosity of spaces that liquid can fill will show a jagged pattern. This can be overcome by increasing the resolution of the XR3DM data sets, or by introducing a routine that performs a sub-element enhancement of the existing data sets. For all three cases, the computational requirements will be greatly increased.

Density Analysis

One objective of this study was to explore the relationship between water spreading and the local density of the fibrous web. Figure 20 and Figure 21 (left column) show the 2D projection of the liquid phase of the various towel samples. In those same figures the final iterations of the simulated water phase is superimposed onto the 3D apparent density map. Apparent density is inversely proportional to the

void space into which the water infiltrates. It was hypothesized that capacity and flow velocity each can benefit from ideal interfiber spacing that is neither too small in volume for a reduction in capacity, nor too large for the liquid to circumvent void spaces. Generally, all 2-ply towels have specific base paper characteristics and embossments that are more significantly densified. CWP towels typically show an MD oscillatory bulking due to the creping process. Crepe lines across the CD cause an MD variability in density and an out-of-plane corrugating effect. Structured towels, such as TAD and ATMOS showed designed patterns of compressed regions as a result of the drying process. The patterns in TAD-1 shown in Figure 20 are easily recognized as densified ovals in the lower center and lower right. The low-density region between these features seems to inhibit flow that readily occurs as the liquid enters the densified region. A similar effect occurs in the upper left where the water phase has not entered the two low-density regions. Volumetric capacity appears lower in the densified embossments as seen in TAD-1, TAD-2 and CWP-2. The correlation between the simulated water phase concentration and local apparent density was examined for these samples, but there seemed to be no direct dependency. However, it is thought that the heterogeneity of the structures, with the various engineered features, i.e. embossments, creped regions, and TAD features, cannot be considered in the aggregate, but should be addressed by partitioning the image [82] so that the liquid movement through each type of structure is examined separately.

Liquid Vacancies

Using the 2D projections of the water phase that are shown in Figures 20 and 21, it was possible to calculate several characteristic parameters for each sample. Initial observations suggested that the size distribution of the pore structure formed by interfiber spacing left regions unfilled with water. Compare the void space pattern for ATMOS and CWP-2 with CWP-3. For each sample, similar patterns were observed in results from both the wetting experiments and the simulation. The 2D projections were used to gain a first approximation of regions that remained free of water. Quantification was based on the areal percentage of vacant space in the wetted region. Figure 22 plots the percentage of vacancies for each of the samples tested. Comparing CWP-1 and CWP-2, grammage is likely an important factor contributing to the larger vacant space observed for CWP-2. However, ATMOS and CWP-1 have similar grammage, so that the formed structure of the ATMOS results in the greatest amount of void space of all samples. The two TAD samples have higher grammage, and as result will be less likely to show through holes in 2D projections. This analysis does not provide a conclusive assessment of inter-fiber spacing and liquid transport potential. A more rigorous analysis can be performed using the 3D data sets that will be considered in future studies.
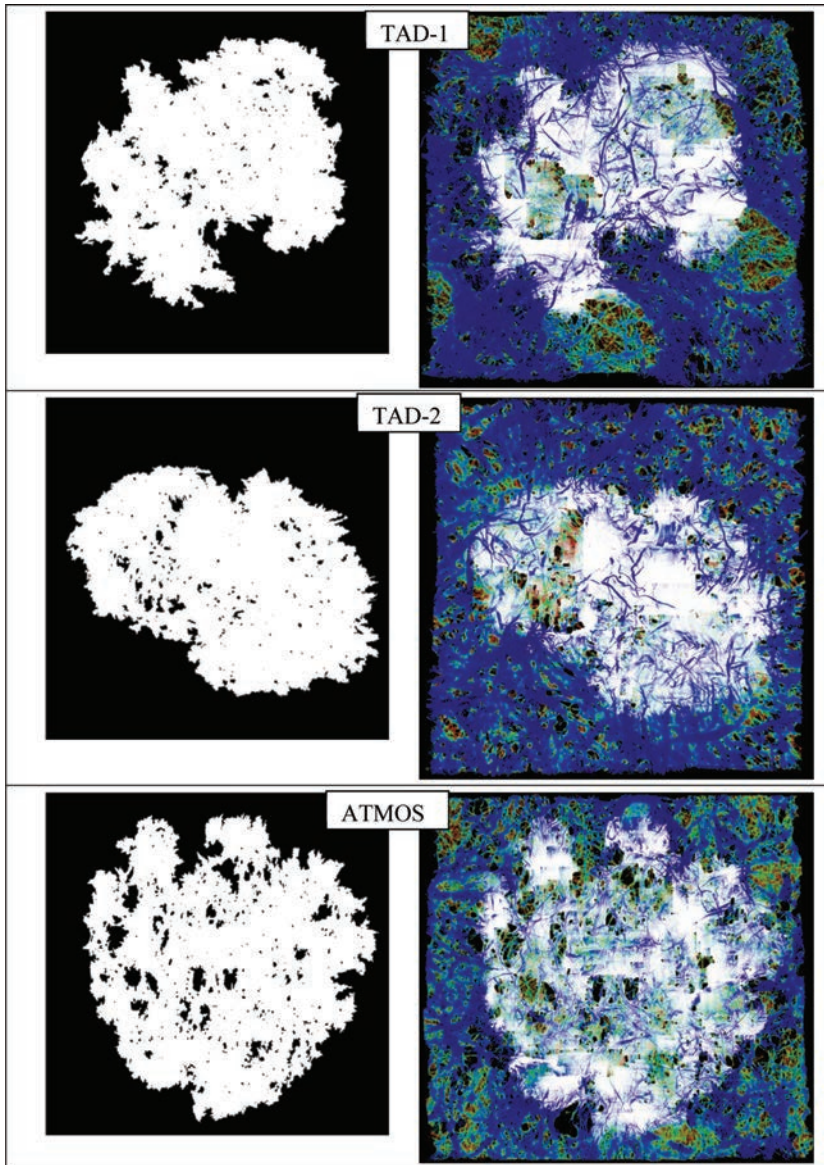
Figure 20. Two-dimensional projections of the wetted region of structured towels generated by the simulated wetting within XR3D tomographic data. The left column shows projections. The right column shows the projections overlaid on a perpendicular view of a 3D map of the local apparent density determined from XR3D tomographic data.
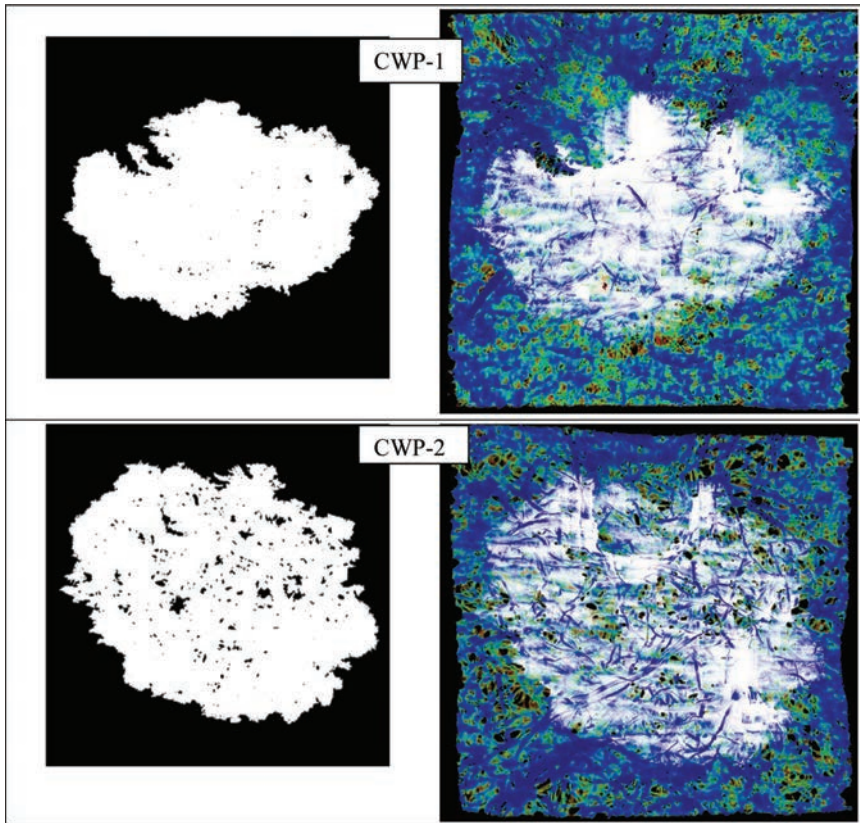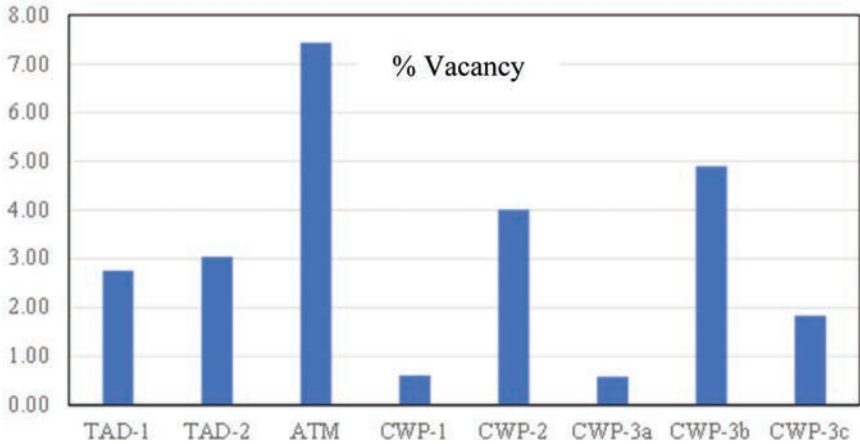
Figure 21. Two-dimensional projections of the wetted region of CWP towels generated by the simulated wetting within XR3D tomographic data. The left column shows projections. The right column shows the projections overlaid on a perpendicular view of a 3D map of the local apparent density determined from XR3D tomographic data.
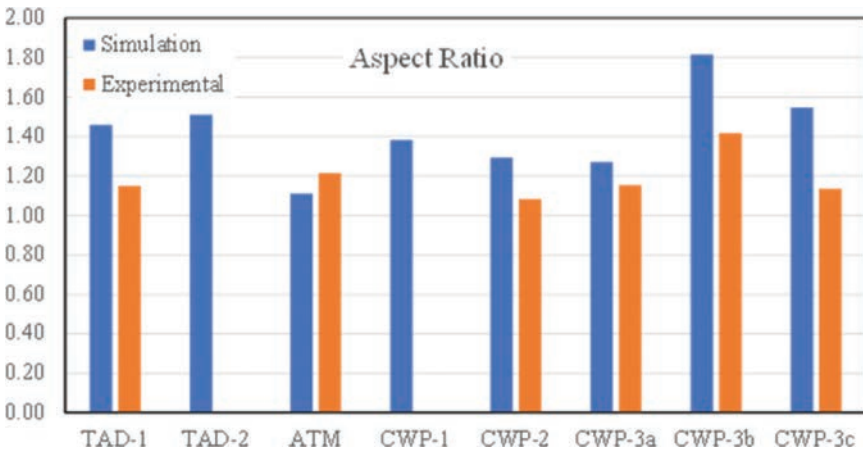
Aspect Ratio

The 2D projections were also used to analyze any existing anisotropy of the wetted region. The key structural properties that should affect anisotropy are fiber orientation, creping and forming or TAD fabrics that introduce directionality in the web. In this study, both aspect ratio and dominant orientation angle were calculated from the 2D projections. The results for orientation for the 5 x 5 mm^2 regions gave inconclusive results that were significantly affected by large features such as embossments. A more elaborate study should be conducted to explore the utility of that parameter. However, aspect ratio has the potential as a direct indi-

Figure 22. The percentage of through hole area to total wetted area determined from the two-dimensional projections of the wetted region for various towel papers as generated by the simulated wetting within XR3D tomographic data.

Figure 23. The calculated aspect ratio of the wetted area for results from μ-wetting experiments and the wetting simulation using XR3D tomographic data.

cator of the effect that creping has on wetting rates and capacity. Figure 23 shows the calculated aspect ratios for all of the samples tested including results obtained from both experimental and simulated 2D images. The experimental results for aspect ratio were lower in all cases as compared to the results produced by the simulation. Also, there does not appear to be a correlation between experimental

and simulation results. Several factors may contribute to this, including a non-uniform buffering response during µ-wetting experiments as fibers swell or the web deforms with the infiltration of water [11, 12, 83]. This model does not account for such structural changes that can effect liquid flow. Considering CWP-1 and CWP-2 samples, water tended to preferentially wick along the creping lines in the cross-machine direction. This can be seen as the density overlays in Figure 21. The anisotropies observed for the two TAD samples appear to result from advancement around larger features and not due to fiber alignments or creping since samples show a dominant diagonal bias corresponding to the location of large features. Additional testing of larger data sets would be useful for identifying the origin of anisotropy in these samples. The simulation results for the ATMOS sample are not useful for characterizing orientation since the XR3D data set had a larger circular embossment near the center. The wetted region conformed to the sidewall of the embossment which is clearly visible in the final iteration image. The spreading pattern of the water phase up to that point reflected flow through the densified region of an embossment and not the structured shape formed during the ATMOS process.

Water Absorbency Capacity

A significant parameter of paper towel products is the water absorbency capacity expressed as mass of water per mass of fiber. Values for two-ply towels typically fall within a range near 10 g/g. Water absorbency capacity (WAC) for all of the single-ply samples in this study were calculated from the wetting simulation results. There was no intent to extrapolate the two-ply performance from single-ply results, since the multi-ply construction and the response of that assembly to water wetting remains unknown. However, WAC for single-ply towels may indirectly provide important insight into performance differences, such as capacity or absorption rate, between towel products. WAC was determined using the 2D wetted area, cf. Figure 20 and 22, to define the boundaries within which water mass was determined from simulation results and fiber mass was determined from the original XR3D data set. The WAC results for the samples from different forming processes are shown in Figure 24. as a function of water phase volume. The bulky structure of the premium grade TAD samples provided more holding capacity than the three other samples that have more densified structures. Once the water phase had saturated the Z-direction void space the WAC curve approached a limit, with the exception of TAD-1. For that sample, the absorption had not yet stabilized when the wetted region reached the external boundary of the data set. Examination of the image of the 3D water phase for the TAD-1 shown in Figure 19 suggests that spreading does not favor simple radial expansion. Rather liquid advances non-uniformly in an irregular branched pattern.

Comparison of Fiber Furnish

The effect of structural changes due to different fiber furnishes was examined by testing CWP towels formed by the same process. Specifically, CWP-3A was made from secondary/recycled pulp, CWP-3B was made from virgin kraft softwood pulp, and CWP-3C was made from sawdust kraft pulp. Thus, the compositions form different pore structures, will densify differently during processing, and are hypothesized to have significantly different wetting behavior. Figure 25 shows the XR3DM tomographic images of the fiber structure and the water phase created in the simulation. In the left column, the overall appearance of the creping structures of the samples appears similar. However, close inspection of the fiber morphology, the apparent density of the structures, and the amount of through holes appear significantly different.

Aspect Ratio

The wetting model generated significantly different patterns of water wicking in response to the web structure. All three samples showed preferential wetting
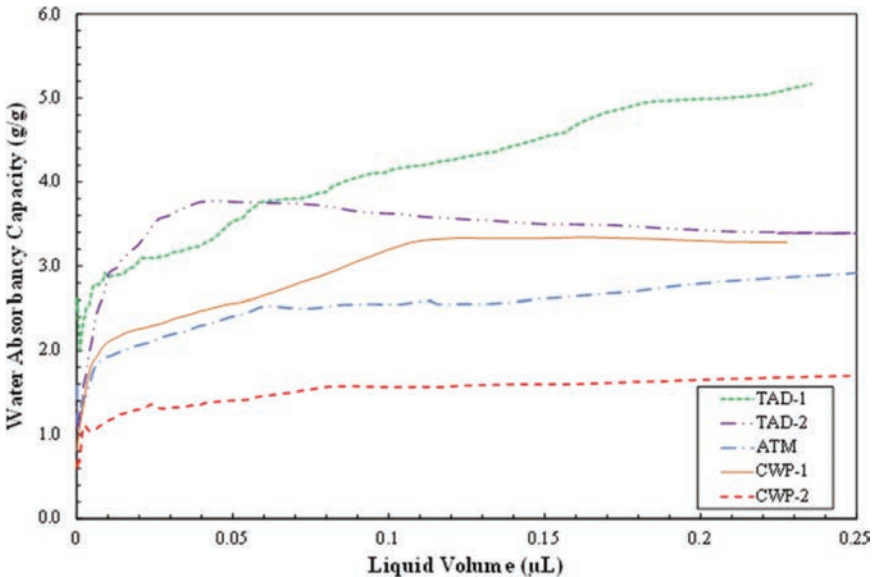
Figure 24. Water holding capacity (WAC) plotted as a function of water phase as generated from the wetting simulation using XR3D tomographic data sets. Samples are the outer ply of various paper towels representing different forming methods.
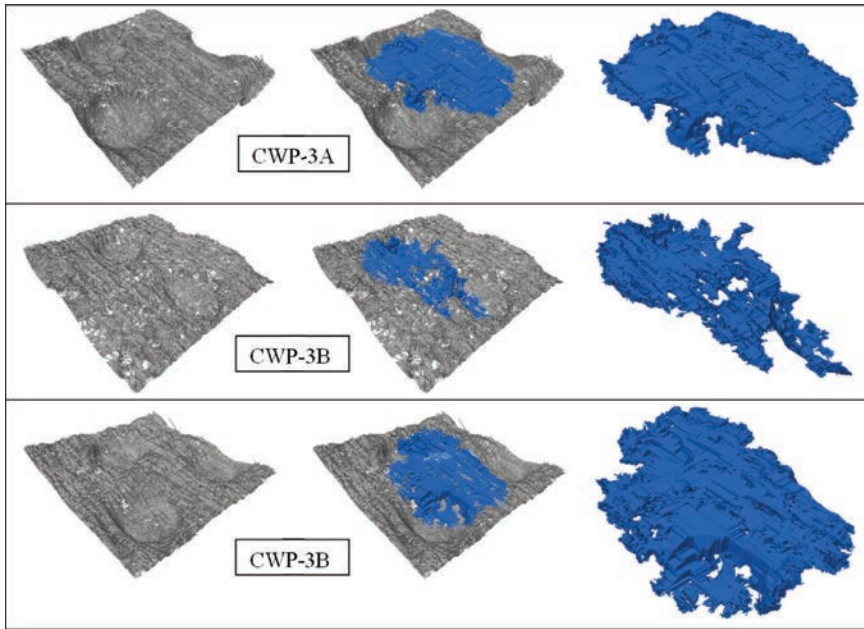
Figure 25. Representations of XR3DM data sets and respective water phase data generated using the wetting smulation for CWP towel samples made from the same fiber furnish. Imaged area is 5 x 5 mm^2 to a resolution of 2.5 μm. Left colum shows tomographs of fibrous structures. Center column shows fiber and water structures together. Right column shows a maginication of the water phase data.

in the cross-machine direction in response to creping lines. Sample CWP-3B with coarse fibers had a much more open fibrous structure and yielded an equally porous wetted region. With the high aspect ratio, less water was introduced before the region reached the outer limits of the sample space. The finer fibers of CWP-3A resulted in a wetted region that spreads radially from the seed location. However, this did not provide the maximum holding capacity. Aspect ratios were calculated and are plotted in Figure 23. The highest value was observed for CWP-3B that had a bulkier structure and coarser fibers. This suggests that creping either bulks the structure more or forms structures more dimensionally conducive to cross machine migration of water. The secondary/recycled pulp had the lowest aspect ratio, which might result from the denser structure and possibly less bulking occurred in the creping process.

Density Analysis

Images of the 2D projections are provided in Figure 26. The differences in response to creping can be seen in the anisotropy of the projected 2D images. Both CWP-3A and CWP-3C have well-formed regions. Wetting is clearly obstructed by embossment, either due to sidewall pore structure or the significant out of plane deformation that occurs in these samples. In general, the density appears relatively uniform in all three samples with the exception of the densified regions of embossments, as seen in the density maps shown in right column of Figure 26.

Liquid Vacancies

The relative area of through holes determined from the 2D projections of the water phase appear quite different for the three samples. Calculated values are plotted in Figure 22 along with all other samples tested in this study. Clearly the virgin kraft pulp showed the most significant open pore space of all of the CWP samples, including the CWP-2 sample that had a lower grammage. This further suggests the significance of fiber cross sectional dimensions, the uniformity thereof, the extent of collapse, and inter fiber spacing that all contribute to the absorption behavior.

Water Absorbency Capacity

The influence of morphological structure on water absorbency capacity (WAC) that was observed for the different forming processes is seen again for samples made from different fiber furnishes. Figure 27 shows a graph of the water absorbency capacity plotted as a function of the volume of water introduced in the simulation. The CWP-3B sample, with the most open porous structure exhibited a lower water absorbing capacity as compared to the other samples. This was likely due to the inability of water to bridge the wide inter-fiber spacing that was apparent from the XR3DM tomographic images. Future work would benefit from characterizing this space from the perspective of cylindrical separation distance of fibers rather than from cylindrical or spherical pore diameter, since many of the towel samples have the void space as the continuous phase. Sample CWP-3C, composed of sawdust kraft pulp had more void spaces than the CWP-3A made from secondary fiber. However, it also exhibited higher WAC values. This can be attributed to having pores that are large enough for capacity, but not sufficiently large to leave liquid vacancies, as was the case for the virgin kraft pulp towel CWP-3B.
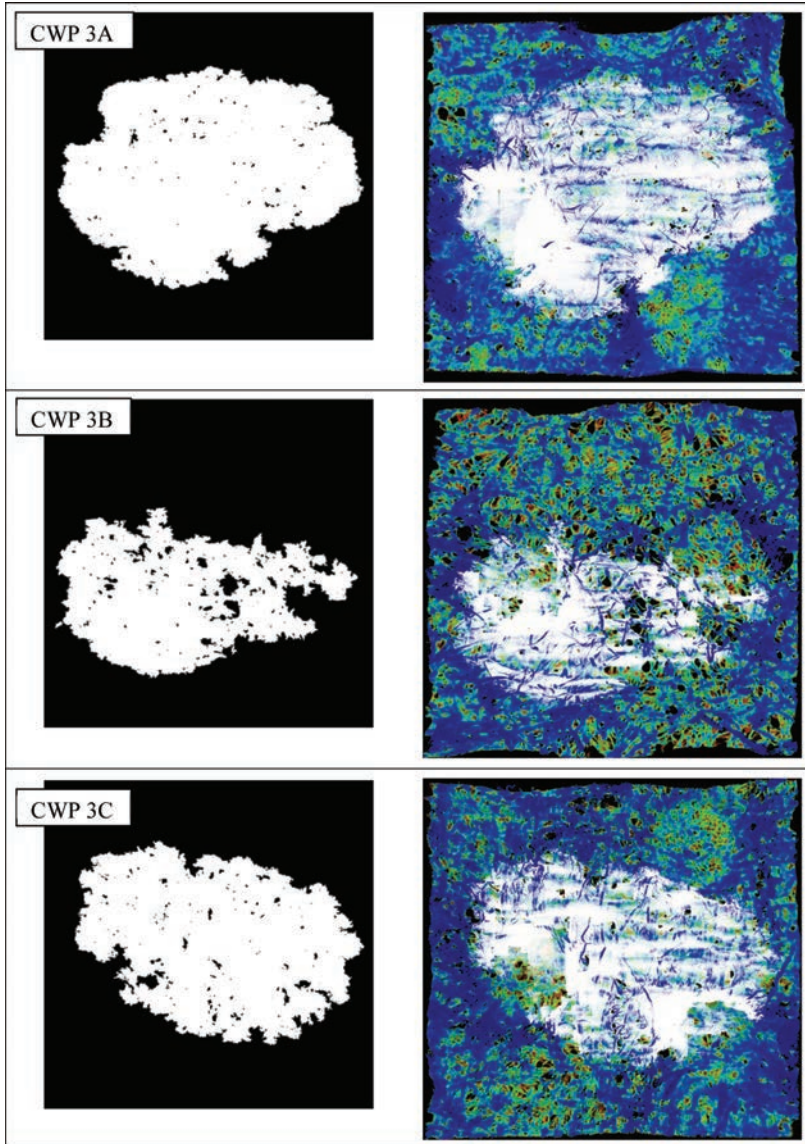
Figure 26. Two-dimensional projections of the wetted region of CWP towels made with differing fiber furnishes as generated by the simulated wetting within XR3D tomographic data. The left column shows projections. The right column shows the projections overlaid on a perpendicular view of a 3D map of the local apparent density determined from XR3D tomographic data.
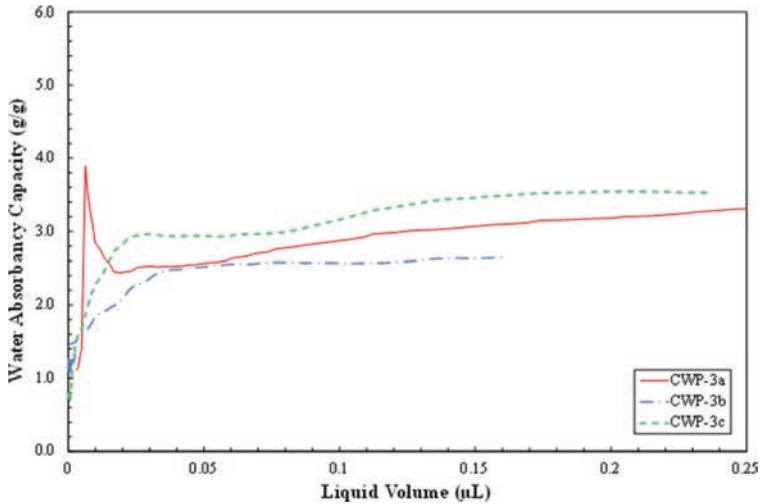
Figure 27. Water holding capacity (WAC) plotted as a function of water phase as generated from the wetting simulation using XR3D tomographic data sets. Samples are the outer ply of towels using the same forming process but with different fiber furnishes.

CONCLUSIONS

In this paper we present the findings of an investigation into the spreading of liquid through low density complex structures using the results from modeling and experimentation. Specifically, retail kitchen towels were used as subject materials for experiments that explored the capillary driven wicking behavior at a resolution on the order of fiber widths, over an area that included numerous induced engineered features such as creping, TAD structuring and embossments. X-ray 3D microscopic data sets acquired from the same towel samples were also used in a numerical model to simulate liquid interaction with the internal fibrous topography as the liquid advances during radial spreading. The results from μ-wetting experiments and the model simulation were compared to structural maps, including thickness, grammage and density. The aim was to examine how each of these affect the local movement at the liquid/void boundary. Spatial and volumetric parameters that characterize the shape, volumetric capacity and amount of vacancies left within the wetted region were calculated from experimental and modeling results for all samples. Comparison between experimental and modeling results was performed to determine the extent to which the model can be used to predict wetting behavior.

A new experimental method was presented for characterizing the wetting behavior of papers, especially those with significant heterogeneity of structure

such as kitchen towels. An experimental apparatus was developed, referred to as the μ-wetting instrument, and used to test samples. The method involved the injection of small volumes of liquid, in this case 2 μL of water, at a fixed injection rate into the sample and then imaging the radial spreading of the liquid as a function of time. An infrared camera was used to capture sequences of thermal images that clearly defined the wet and dry regions at a resolution of about 50 μm, over an area of about 20x20 mm². Towel samples formed by through air drying (TAD), ATMOS, and conventional wet pressed (CWP) were tested. For the TAD sample, wetting appeared to advance most rapidly in the high density regions and appeared to slow around embossments. This produced an irregular wet/dry perimeter. The wetted area was less than the other two samples for the same delivery volume indicating that it had a greater water holding capacity expressed as g/g. The radial spreading of water in the CWP showed the most circular pattern that slowed significantly around out-of-plane features such as embossments. The wetted region expanded more in the cross machine direction, likely resulting from preferential wicking along creping lines. The structured ATMOS sample had a significant amount of large through-holes in the structure that did not fill with water during wetting. The water holding capacity was lower than the TAD but comparable to the CWP samples.

The effect of fiber furnish was also tested in μ-wetting experiments. Three CWP samples made from different pulps were made using the same manufacturing process to the same product specifications. Samples made from kraft pulped sawdust and secondary fiber both had finer fiber length distributions. Both samples showed well defined radial wetting patterns that advanced preferentially in the cross machine direction and were slowed only by embossed features. The sample made from virgin kraft pulp had more internal vacancies that did not wet and showed a more irregular periphery disrupted by out-of-plane features. The local velocity of liquid as it advanced through the structure was calculated for all samples using the sequence of images collected during the wetting experiments. Representations provide insight into the rate changes as structural differences were encountered during the wicking process. Future work should focus on registering the local velocity maps with grammage or density maps and by segmenting different structural regimes to quantify the relationship between structure and flow velocity.

A numerical model based on local interfacial interaction energy was developed to provide a qualitative indication of the preferential advancement of a liquid front through 3D representations of low density fibrous structures. X-ray 3D tomographic data sets were obtained for a series of kitchen towel samples including those tested in μ-wetting experiments. The model cycles through the testing of each element within the 3D sample space that is at the liquid/void boundary to determine if energy is reduced then the element is changed from liquid to void or

vice versa. The total interaction energy for each element is determined by summing the interaction energies between that element and the 18 neighbors in direct contact that are either liquid, solid or void. Therefore, advancement of the liquid front at any location is influenced by the three phase topography of the surrounding neighborhood. Controlling factors include interfiber separation, the surface tension of the liquid and the geometry that the liquid forms on irregular surfaces. The model only considered the topography local to each element in contact with the liquid phase, and disregarded hydrodynamics, viscous flow, and global energetic balance of the liquid phase.

The simulation was initiated with a small seed region of liquid placed in the sample center and proceeded to simulate radial wetting of the samples. Significant differences were observed between the wetted regions generated for the TAD, ATMOS and CWP samples. Spreading behavior appeared consistent with the wicking patterns observed in μ-wetting experiments. The TAD sample produced a highly branched and irregular spreading front and was confined to a smaller area. Calculation of the water holding capacity gave values nearly twice as high, 5 g/g, as the CWP samples, 2.5–3.0 g/g. The ATMOS sample had similar water holding capacity as the CWP samples. The spreading pattern for the ATMOS and CWP samples was generally circular with an aspect ratio of 1.3–1.8, respectively, biased in the cross machine direction due to response to the creping lines. CWP samples formed from pulps that had high concentrations of fines, i.e. secondary pulp or sawdust kraft pulp, had very few vacancies within the wetted region, suggesting that interfiber distances were small enough to enable water to bridge the spacing and fill the void. The CWP sample made from virgin kraft pulp and the ATMOS sample showed much larger vacancies in the wetted region which appeared to have a negative impact on water holding capacity. Local apparent density maps were generated for all towel samples from the XR3DM data sets using a procedure that determines density oriented from the center surface maps. Wetted regions were overlaid on density maps to qualitatively assess the relationship between density and the simulated migration through the structures. It was observed that the liquid advanced through specific regions that were denser and avoided regions with void spaces that seemed to exceed a certain size leaving non-wetted vacancies throughout. The amount of vacant space within the wetted region was found to depend on both forming process and fiber furnish.

Future work will investigate spreading that occurs in specific regions, such as only the embossed or non-embossed regions, or omitting embossments to observe only creped regions alone. Quantification of liquid advance as a function of interfiber spacing will be attempted by studying the morphology of the 3D wetted region. These methods will also be valuable in the investigation of other systems with different chemistries and structures such as other liquids and nonwoven materials.

ACKNOWLEDGEMENTS

REFERENCES

[1] P. Tardiff. Nibroc Paper Towels Ii. In *Once Upon a Berlin Time*, (ed.), pp. 189–192, AuthorHouse, Bloomington, Ind, 2003.

[2] R. Spector and W.W. Wicks. *Shared Values: A History of Kimberly-Clark*, Greenwich Publishing Group 1997.

[3] B. Gordon. One of the Most Valuable Fabrics': The Seemingly Limitless Promise of Crepe Paper, 1890–1935. *Ars Textrina* 31 (1):107–144, 1999.

[4] E.R. Wells. Compressible Laminated Paper Structure. Procter and Gamble Co, United States Patent US3414459A, 1968.

[5] L.H. Sanford and J.B. Sisson. Process for Forming Absorbent Paper by Imprinting a Fabric Knuckle Pattern Thereon Prior to Drying and Paper Thereof. United States Patent US3301746A, 1967.

[6] G. Forest. Apparatus for Forming High Bulk Tissue Having a Pattern Imprinted Thereon. Beloit Corp, United States Patent US3629056A, 1969.

[7] T. De Assis, L.W. Reisinger, L. Pal, J. Pawlak, H. Jameel and R.W. Gonzalez. Understanding the Effect of Machine Technology and Cellulosic Fibers on Tissue Properties–a Review. *Bioresources* 13(2):4593–4629, 2018.

[8] B. Janda. Sheet Structure Process Effect on Tissue Properties. *TAPPI Tissue360°* 4(1):16–23, 2015.

[9] T. Young. Iii. An Essay on the Cohesion of Fluids. *Philosophical transactions of the royal society of London* (95):65–87, 1805.

[10] S. Chang, J. Seo, S. Hong, D.-G. Lee and W. Kim. Dynamics of Liquid Imbibition through Paper with Intra-Fibre Pores. *Journal of Fluid Mechanics* 845:36–50, 2018.

[11] B. Nasouri, B. Thorne and G.J. Elfring. Dynamics of Poroelastocapillary Rise. *Journal of Fluids and Structures* 85:220–228, 2019.

[12] M. Kvick, D.M. Martinez, D.R. Hewitt and N.J. Balmforth. Imbibition with Swelling: Capillary Rise in Thin Deformable Porous Media. *Physical Review Fluids* 2(7):074001, 2017.

[13] Tappi. Water Absorbency of Bibulous Papers.T 432 cm-21, TAPPI, Atlantsa, GA, 2021.

[14] Iso. Tissue Paper and Tissue Products. In *Part 8: Water-absorption time and water-absorption capacity, basket-immersion test method*, 12625–8:2010, p. 7, 2010.

[15] D. Danino and A. Marmur. Radial Capillary Penetration into Paper: Limited and Unlimited Liquid Reservoirs. *Journal of Colloid and Interface Science* 166(1): 245–250, 1994.

[16] Iso. Determination of Capillary Rise – Klemm Method. In *Paper and Board,* 8787, 1986.

[17] M. Parada, D. Derome, R. Rossi and J. Carmeliet. A Review on Advanced Imaging Technologies for the Quantification of Wicking in Textiles. *Textile Research Journal* 87(1):110–132, 2017.

[18] S.G. Reid. A Method of Measuring the Rate of Absorptionof Water by Creped Tissue Paper. *Pulp and Paper Mag. Canada* 68(3):T115-T117, 1967.

[19] M.K.S. Inc. The M/K Gats Model 1200 Absorbency Tester. M/K Systems Inc., https://mksystems.com/mk-gats-liquid-absorbency-system/, 2022.

[20] Iso. Demand Absorbency. In *Textiles — Test methods for nonwovens,* 9073–12:2002, pp. 1–12, International Organization for Standardization, Geneva, 2019.

[21] S.I. Inc. Absorbency Testing System. 2022, Sherwood Instruments Inc, Lynnfield, MA, 2012.

[22] P.D. Beuther and M.W. Veith. Sources of Variability in Testing Absorptive Rate of Tissue Paper. In *TAPPI Engineering, Pulping, & Environmental Conf.,* vol. 1, pp. 1–12, TAPPI Press, Memphis, TN, 2009.

[23] Tappi. Sorptive Rate and Capacity of Bibulous Paper Products, Using Gravimetric Prinicples. T-561-pm, TAPPI Press, 1996.

[24] D. Loebker and J. Sheehan. Paper Towel Absorptive Properties and Measurement Using a Horizontal Gravimetric Device. In *TAPPI PaperCon 2011,* pp. 1210–1218, TAPPI Press, Covington, KY, 2011.

[25] P.D. Beuther, M.W. Veith and K.J. Zwick. Characterization of Absorbent Flow Rate in Towel and Tissue. *J Eng Fiber Fabr* 5(2):1–7, 2010.

[26] A. Gabrielsson, H. Vomhoff and A. Tysen. Investigation of the Dynamic Liquid Absorption Properties of Kitchen Towel. In *TAPPI PaperCon 2014,* pp. 3137–3160, TAPPI Press, Nashville, TN, 2014.

[27] K. Olejnik, P. Pełczyński, M. Bogucka and A. Głowacka. Optical Measurement of the Hydrophobic Properties of Paper Products. *Measurement* 115:52–63, 2018.

[28] K. Olejnik, J.-F. Bloch and P. Pelczynski. Measurement of the Dynamics of Fluid Sorption for Tissue Papers. *TAPPI JOURNAL* 18(7):417–426, 2019.

[29] F.P. Morais, J.C. Vieira, A.O. Mendes, A.M. Carta, A.P. Costa, P.T. Fiadeiro, J.M. Curto and M.E. Amaral. Characterization of Absorbency Properties on Tissue Paper Materials with and without "Deco" and "Micro" Embossing Patterns. *Cellulose* 29(1):541–555, 2022.

[30] A. De Oliveira Mendes, P.T. Fiadeiro, A.M.M. Ramos and S.C.L. De Sousa. Development of an Optical System for Analysis of the Ink–Paper Interaction. *Machine Vis. Apps.* 24(8):1733–1750, 2013.

[31] M.A. Hubbe, D.J. Gardner and W. Shen. Contact Angles and Wettability of Cellulosic Surfaces: A Review of Proposed Mechanisms and Test Strategies. *Bioresources* 10(4):8657–8749, 2015.

[32] R.A. Young. Wettability of Wood Pulp Fibers: Applicability of Methodology. *Wood Fiber Sci* 8(2):120–128, 1976.

[33] K.T. Hodgson and J.C. Berg. Dynamic Wettability Properties of Single Wood Pulp Fibers and Their Relationship to Absorbency. *Wood Fiber Sci* 20(1):3–17, 1988.

[34] J. H. Klungness. **Measuring the Wetting Angle and Perimeter of Single Wood Pulp Fibers: A Modified Method**, vol. 64 1981.

[35] N. Yoshinaga, T. Okayama and R. Oye. Measurement on Wettability of Pulp Fiber at Short Time Intervals. *Sen'i Gakkaishi* 49(6):287–293, 1993.

[36] H. Jin, R. Kose, N. Akada and T. Okayama. Relationship between Wettability of Pulp Fibers and Tensile Strength of Paper During Recycling. *Sci Rep-Uk* 12(1):1–11, 2022.

[37] L. Wilhelmy. Wilhelmy Plate Method. *Ann. Phys* 119:117, 1863.

[38] B. Miller and R.A. Young. Methodology for Studying the Wettability of Filaments. *Textile Research Journal* 45(5):359–365, 1975.

[39] H. El Omari, E.-H. Ablouh, F. Brouillette, M. Taourirte and A. Belfkira. New Method for Determining Paper Surface Energy Per Contact Angle. *Cellulose* 26(17):9295–9309, 2019.

[40] A. Liukkonen. Contact Angle of Water on Paper Components: Sessile Drops Versus Environmental Scanning Electron Microscope Measurements. *Scanning* 19(6):411–415, 1997.

[41] S. Martinis, J. Ferris, P. Balousek and M. Beetham. Absorption of Liquids by Dry Fiber Networks. In *TAPPI Annual Meeting, Chicago*, 1981.

[42] N. Pan and W. Zhong. Fluid Transport Phenomena in Fibrous Materials. *Textile Progress* 38(2):1–93, 2006.

[43] A. Patnaik, R. Rengasamy, V. Kothari and A. Ghosh. Wetting and Wicking in Fibrous Materials. *Textile Progress* 38(1):1–105, 2006.

[44] E.W. Washburn. The Dynamics of Capillary Flow. *Physical Review* 17(3):273–283, 1921.

[45] T. Gillespie. The Capillary Rise of a Liquid in a Vertical Strip of Filter Paper. *Journal of Colloid Science* 14(2):123–130, 1959.

[46] J. Hyväluoma, P. Raiskinmäki, A. Jäsberg, A. Koponen, M. Kataja and J. Timonen. Simulation of Liquid Penetration in Paper. *Physical Review E* 73(3):036705, 2006.

[47] J. Philip. Flow in Porous Media. *Annual Review of Fluid Mechanics* 2(1):177–204, 1970.

[48] N. Mao and S.J. Russell. Anisotropic Liquid Absorption in Homogeneous Two-Dimensional Nonwoven Structures. *J Appl Phys* 94(6):4135–4138, 2003.

[49] S. Jaganathan, H.V. Tafreshi and B. Pourdeyhimi. A Realistic Modeling of Fluid Infiltration in Thin Fibrous Sheets. *J Appl Phys* 105(11):113522, 2009.

[50] S. Jaganathan, H.V. Tafreshi and B. Pourdeyhimi. Two-Scale Modeling Approach to Predict Permeability of Fibrous Media. *J Eng Fiber Fabr* 3(2) 2008.

[51] L.A. Richards. Capillary Conduction of Liquids through Porous Mediums. *Physics* 1(5):318–333, 1931.

[52] A. Ashari, T.M. Bucher and H. Vahedi Tafreshi. A Semi-Analytical Model for Simulating Fluid Transport in Multi-Layered Fibrous Sheets Made up of Solid and Porous Fibers. *Computational Materials Science* 50(2):378–390, 2010.

[53] A. Ashari, T.M. Bucher, H.V. Tafreshi, M.A. Tahir and M.S.A. Rahman. Modeling Fluid Spread in Thin Fibrous Sheets: Effects of Fiber Orientation. *Int J Heat Mass Tran* 53(9–10):1750–1758, 2010.

[54] S. Succi. **The Lattice Boltzmann Equation: For Fluid Dynamics and Beyond**, Oxford university press 2001.

[55] X. Shan and H. Chen. Lattice Boltzmann Model for Simulating Flows with Multiple Phases and Components. *Phys Rev E Stat Phys Plasmas Fluids Relat Interdiscip Topics* 47(3):1815–1819, 1993.

[56] A. Moghadam, M. Jamali, D.G. Venkateshan, H.V. Tafreshi and B. Pourdeyhimi. A New Approach to Modeling Liquid Intrusion in Hydrophobic Fibrous Membranes with Heterogeneous Wettabilities. *Colloids and Surfaces a-Physicochemical and Engineering Aspects* 558:154–163, 2018.

[57] A. Bakhta, S. Leclaire, D. Vidal, F. Bertrand and M. Cheriet. Multiscale Simulation of Ink Seepage into Paper: A Mesoscopic Variational Model. *Comput Phys Commun* 239:1–13, 2019.

[58] D. Lukas, E. Kostakova and A. Sarkar. Computer Simulation of Moisture Transport in Fibrous Materials. In **Thermal and Moisture Transport in Fibrous Materials**, pp. 469–541, 2006.

[59] M. Weng and D. Lukas. A Stochastic Study on the Wicking Phenomena. *J. Donghus Univ.* 29(2):178–181, 2012.

[60] E. Ising. Contribution to the Theory of Ferromagnetism. *Z. Phys* 31(1):253–258, 1925.

[61] D. Lukas, N. Pan, A. Sarkar, M. Weng, J. Chaloupek, E. Kostakova, L. Ocheretna, P. Mikes, M. Pociute and E. Amler. Auto-Model Based Computer Simulation of Plateau-Rayleigh Instability of Mixtures of Immiscible Liquids. *Physica a-Statistical Mechanics and Its Applications* 389(11):2164–2176, 2010.

[62] D. Lukas and N. Pan. Wetting of a Fiber Bundle in Fibrous Structures. *Polym Composite* 24(3):314–322, 2003.

[63] W. Zhong, N. Pan and D. Lukas. Multi-Scale Modeling of Liquid Tranport in Fibrous Materials. In *Computational Fluid and Solid Mechanics 2005*, (ed. K.J. Bathe), pp. 954–957, Boston, MA. MIT, 2005.

[64] D. Lukas, V. Soukupova, N. Pan and D.V. Parikh. Computer Simulation of 3-D Liquid Transport in Fibrous Materials. *Simul-T Soc Mod Sim* 80(11):547–557, 2004.

[65] W. Zhong, N. Pan and D. Lukas. Stochastic Modelling of Tear Behaviour of Coated Fabrics. *Model Simul Mater Sc* 12(2):293–309, 2004.

[66] R.F. Moghaddam, F.F. Moghaddam and M. Cheriet. Computer Simulation of 3-D Finite-Volume Liquid Transport in Fibrous Materials: A Physical Model for Ink Seepage into Paper. *arXiv preprint arXiv:1307.2789* 2013.

[67] Tappi. Standard Conditioning and Testing Atmospheres for Paper, Board, Pulp Handsheets, and Related Products. T-402 sp-08, TAPPI, Atlantsa, GA, 2008.

[68] Tappi. Grammage of Paper and Paperboard (Weight Per Unit Area). T410 om-02, TAPPI PRESS, Atlanta, 2003.

[69] D.S. Keller, C. Feng, J.F. Bloch and S. Rolland Du Roscoat. Local Structural Orientation of Towel and Tissue Grades. In *15th Fundamental Reseasrch Symposium*,

(ed. S. I'anson), p. 3, Cambridge, UK. The Pulp and Paper Fundamental Research Society, UK, 2013.

[70] D.S. Keller, G. Wang and C. Feng. Structural Properties and Compressive Response of Hygienic Papers. In *2016 PAN PACIFIC CONFERENCE of the Korean Technical Associations of the Pulp and Paper Industry*, Seoul, Korea. Korean Technical Associations of the Pulp and Paper Industry, 2016.

[71] D.S. Keller and J.J. Pawlak. Beta-Radiographic Imaging of Paper Formation Using Storage Phosphor Screens. *Journal of Pulp and Paper Science* 27(4):117–123, 2001.

[72] T.M. Cresson, H. Tomimasu and P. Luner. Characterization of Paper Formation .1. Sensing Paper Formation. *Tappi Journal* 73(7):153–159, 1990.

[73] W.K. Ng and C.T.J. Dodson. Rapid Formation Performance Test in Proceedings Int. Paper Phys. Conf Niagara-on-the-Lake, ON: TAPPI Press, pp. 49–53, 1995.

[74] C. Feng. Soft X-Ray Measurement of Low Densitymaterials and Compressive Response Characterization, M.S. Thesis, Chemical and paper Engineering, Miami University, Oxford, Ohio, 2012.

[75] Y.J. Sung, C.H. Ham, O. Kwon, H.L. Lee and D.S. Keller. Applications of Thickness and Apparent Density Mapping by Laser Profilometry. In *Advances in Paper Science and Technology: Trans. 13th Fundamental Research SymposiumCambridge*, (ed. S.J. I'anson), pp. 961–1007, Cambridge, UK. The Pulp and Paper Funmdamental Research Society, 2005.

[76] D. Branca. **Uniformity of Low Density Fibrous Structures and the Effects of Manufacturing Processes on Apparent Density**, SUNY College of ESF 2007.

[77] D.S. Keller, S.R. Du Roscoat and Y. Huang. Mapping the Z-Direction of Mass of Paper Towel Grades Using X-Ray Microtomography. In *2010 Progress in Paper Physics Seminar,*ed, (ed. N. Gurnagul), FP Innovations, Montreal, 2010.

[78] D.S. Keller and H. Abedsoltan. Mesoscale Liquid Absorption Properties of Towel Papers. In *Int. Paper Physics Conf.*, Indianapolis. TAPPI, 2019.

[79] H. Abedsoltan. An Experimental Method to Study the Absorption Capacity of Paper Towels. *TAPPI JOURNAL* 20(4):265–274, 2021.

[80] H. Abedsoltan. Meso-Scale Wetting of Paper Towels, M.S. Thesis, Miami University, 2017.

[81] W.M. Haynes, D.R. Lide and T.J. Bruno. **Crc Handbook of Chemistry and Physics**, Taylor & Francis Group, Boca Raton 2014.

[82] D.S. Keller, D. Branca and O. Kwon. Spatial Partitioning of the Structural Properties of Tissue and Towel Grades. *Advances in Pulp and Paper Research, Oxford 2009, Vols 1–3*:693-+, 2009.

MESOSCALE WATER WETTING OF LOW-DENSITY FIBROUS STRUCTURES: EXPERIMENTATION AND SIMULATION

D. Steven Keller[1]*, H. Abedsoltan*[1]*, J. Reid*[1] *and L. Yin*[2]

[1] Miami University, Department of Chemical, Paper and Biomedical Engineering, Oxford, OH, USA
[2] Beckman Institute, University of Illinois at Urbana-Champaign, Urbana, IL, USA

Shubham Agarwal   University of British Columbia

Does your model also show that most of the water flows into the lumen as compared to the interstitial sites?

Steve Keller

It depends on the diameter of the lumen, but if the lumen is accessible, it readily flows in the lumen.

Shubham Agarwal

So, does it mean that if we keep on increasing the grammage, its water absorbency capacity will increase as more lumen is available?

Steve Keller

The problem with a lot of these samples is there is not a lot of lumens available since they all collapsed, because that is the nature of the kraft fibres found in these

Discussion

commercial papers. So, worrying about the lumen I think is kind of old school for tissues made from mechanical pulps. But going to the second part of your question.

Shubham Agarwal

If we keep on increasing the grammage of the paper, does it mean that its water absorbing capacity will increase monotonically?

Steve Keller

Absolutely. What it does is, you are talking about thickness and this is a three-dimensional expansion. So, if you increase the grammage, you are going to increase the capacity.

Ward Ostendorf   The Procter and Gamble Company

I have 2 comments and questions for you, and then actually I have one for the community. First of all, I love your approach to the model. One thing I love about models, and I think someone alluded to earlier is, you know what physics you have put in, and you know what physics you have not put in, as long as you have thought through the problem. So, I love all the steps you have there, first of all, so that is fantastic in terms of how you built it up in MATLAB. Have you given any thought about doing something through OpenFOAM, which is open source software?

Steve Keller

I am just trying to get the code to run efficiently and bring it closer to a real system.

Ward Ostendorft

That's fine. It is just another tool out there in the modelling community and it does fluids.

Steve Keller

I think I lost half my hair on the parallelisation of the code.

Ward Ostendorf

I was actually just curious if you thought about it. And if you thought about any differences. I love what you have done. Yes, I was just curious if you had considered it.

Steve Keller

I would be worried about it because sometimes when you give a chainsaw to a 5-year-old, they have no idea how to use it. And in this case, the user must understand both the code and what is going on with the science inside, and not just code implementation.

Ward Ostendorf

And then the other thing, I am curious on your perspective, and this is not a commentary on the micro CT, but it is a big challenge handling those datasets. It appears there was some missing mass amongst the fibres. There are spots along what look like the softwood where the cell wall was gone. Is this just the resolution? How much of a difference do you think that makes in your simulations or is it lost in them?

Steve Keller

I don't know if I mentioned that here, but I definitely mentioned that in the paper. Segmentation is a critical aspect of this simulation, absolutely. And in fact, part of my work in the future is to test different segmentation methods, and just see what impact this has on the results. because segmentation defines the diameter of the pores that are provided to liquid spreading in this model. And so, if you over segment and reduce the fibre cell wall, you are going to change pore sizes and channels and so that is absolutely true. And in fact, I have three segmentation processes on hand that I am presently looking at. And I looked at the microCT community to see if they have a great segmentation process, but every time we inquire, there are very few people working specifically on wood-based fibres. Sabine Rolland du Roscoat has been a big help in this regard.

Ward Ostendorf

Now, I've got a question to the community. How many folks are familiar with InterPore? I highly suggest, particularly in this area, that it is a connection to make. It is the international porous media society and they run a yearly conference. One

Discussion

of the critical areas they cove is the holy grail of porous media, which is deformable porous media and nobody has completely solved it yet. But that is a community that has a sub chapter on this area. The challenge is dealing with the issue that of part of it is saturated flow, part of it unsaturated, and you have to account for both. We have talked a lot about capillary pressure, which is a function of saturation. Permeability is also a function of saturation, and it is a piece that often gets lost and is where a lot of the error in the models and the calculations can come in. So anyway, I would encourage, however we might want to do it, some connections between the communities. I believe their next conference is in May 2023 in Edinburgh.

Thomas Harter   Graz University of Technology

I have a question about your wetting experiments. You did simultaneous measurements with a CCD camera and an infrared camera, right?

Steve Keller

No.

Thomas Harter

You did not?

Steve Keller

Oh, that is the infra-red camera that measures temperature gradient and so what I was focusing on was delineation of the parameter of the wet-dry region, which I found impossible other than doing it with the infrared or using a dye, which contaminated the liquid.

Thomas Harter

Yes, that is what I was thinking about. I was interested, if you have ever seen differences when you are doing the same experiment and monitoring it with an optical sensor and watching it with an infrared sensor.

Steve Keller

Oh yes, because the optical sensor does not provide the contrast sufficiently to see individual fibres. What that means is I can change the pH or add surfactants or the

liquid and still be able to image the wetting front. If I change the pH of a dye, it will potentially precipitate and I will see differences that cannot attributed to the surface interaction alone.

Thomas Harter

The thing that I was thinking about is that you detect a difference when using the infrared sensor. There was this work, and I think someone showed it already today, by Murali et.al. where they used the infrared sensor to watch imbibition on the surface. There the infrared signals show high temperature spikes in front of the optical visible liquid front. That is why I was asking: I think the infrared camera is not observing the same as the optical sensor. So, I would guess that there is a difference in your experiment setup between the two observation methods.

Steve Keller

Yes, I am just interested in where the advancing front is at very fine length scales. Okay so, because I cannot observe the heat of wetting in images it does not mean it does not exist, and so that allows me to delineate wet and dry regions. There is an advancing front and the question is whether there is a vapour front in the front of that. I thought the advanced gradient was indicative of vapour, but because it represents cooler temperature then apparently, it is not. So, in these experiments one cannot see a temperature increase. However, Vomhoff did observe increased heat in a similar experimental setup, but that was in a constrained plate. He attributed it to the heat of wetting. I did not observe heat of wetting in the open-air tests of our system.

Thomas Harter

Why would you guess it does not show you the heat of wetting?

Steve Keller

Because I do not see any temperature values that exceed background. So, heat of wetting would have to be above that unless it is being counteracted by a larger cooling effect, so I do not know.

Markus Biesalski   Technical University of Darmstadt

Although you mention that you did not look yet into dynamics with the model, it would be extremely interesting to see, because you have within the one sheet

Discussion

areas that were compressed. Can you see whether the dynamics change when imbibing in this area as opposed to other areas, and whether you can actually model it?

Steve Keller

I think the current model alludes to dynamics in some respects, only because if the liquid is given the opportunity to proceed into a densified region or a region that has optimal pore size, it will follow the most energetically favourable route. However, that is an instantaneous and highly localised action. The moment one considers dynamics you need to consider fluid viscosity, shear rate, the thickness of the layers of liquid at each interface and suddenly the model becomes infinitely complex.

Markus Biesalski

Then, I was about to ask about the meniscus shapes that you mentioned, but there was already a suggestion to use OpenFOAM that can be easily used for something like this.

Steve Keller

I tried to use SurfFit and that also works on a very small scale, but cannot be used for systems as complex as the multi-gigabyte tomographic data sets from this work.